A conservative integration of the pseudo-incompressible equations with implicit turbulence parameterization

Felix Rieper *

Institut für Atmosphäre und Umwelt, Goethe-Universität Frankfurt, Germany

Stefan Hickel

Lehrstuhl für Aerodynamik und Strömungsmechanik, TU München, Germany

Ulrich Achatz

Institut für Atmosphäre und Umwelt, Goethe-Universität Frankfurt, Germany

* *Corresponding author address:* Felix Rieper, Deutscher Wetterdienst, Frankfurter Str. 135, D-63067 Offenbach, Germany

E-mail: felix.rieper@dwd.de

ABSTRACT

Durran's pseudo-incompressible equations are integrated in a mass and momentum conserving way with a new implicit turbulence model. This system is sound-proof, which has two major advantages over fully compressible systems: the CFL condition for stable time advancement is no longer dictated by the speed of sound and all waves in the model are clearly gravity waves (GW). Thus, the pseudo-incompressible equations are an ideal laboratory model for studying GW generation, propagation and breaking. Gravity wave breaking creates turbulence which needs to be parameterised. For the first time the adaptive local deconvolution method (ALDM) for implicit large eddy simulation (ILES) is applied to non-Boussinesq stratified flows. ALDM provides a turbulence model that is fully merged with the discretisation of the flux function. In the context of non-Boussinesq stratified flows this poses some new numerical challenges, the solution of which we present in this text. In numerical test cases we show the agreement of the results with the literature (Robert's hot/cold bubble test case), we present the sensitivity to the model's resolution and discretisation and demonstrate qualitatively the behaviour of the implicit turbulence model for a 2D breaking gravity wave packet.

1. Introduction

A main effect of acoustic waves in the atmosphere is a rapid adjustment to a balanced state with respect to pressure-density perturbations. As long as one is not interested in this adjustment process itself but rather in atmospheric dynamics on comparatively longer time scales, it is often attractive to filter acoustic waves from the dynamic equations. Thus simplified, i.e. soundproof, equations enable a focus on the dynamics of more significant mesoscale processes, while the absence of fast waves also allows for larger time steps in numerical integrations. A classical example is the Boussinesq system, where the prognostic continuity equation is replaced by a diagnostic divergence constraint on the wind field. This yields a good approximation of atmospheric dynamics on spatial scales smaller than the atmospheric scale height. Deep convection and wave propagation, however, experience effects of the vertical decrease of ambient density that cannot be reproduced in the Boussinesq approximation. This density effect causes, e. g. , gravity waves, typically generated in the troposphere, to grow in amplitude until they get unstable, break, and finally dissipate and interact with the large-scale flow in the middle atmosphere (Lindzen 1981; Fritts and Alexander 2003). To include such effects, two more general approaches have been proposed. One is the well-known anelastic equations first introduced by Batchelor (1953) and Ogura and Phillips (1962), and further developed by Lipps and Hemler (1982) and Lipps (1990). They use a more general divergence constraint, which takes the decreasing background density into account as a weighting factor for the wind. A potential drawback of the anelastic system is that it requires the leading-order background atmosphere to be close to isentropic. Some indications exist that corresponding errors might often be negligible even for realistic tropospheric stratifications (Smolarkiewicz and Dörnbrack 2008; Klein et al. 2010; Smolarkiewicz and Szmelter 2011). However, an approach that does not constrain the background potential temperature as much as in the anelastic equations is offered by the pseudo-incompressible system (Durran 1989; Durran and Arakawa 2007; Durran 2008). By introducing the so-called pseudo-incompressible density, the compressible coupling between pressure and density fluctuations

and thus the transfer from elastic potential to kinetic energy is cut off. Smolarkiewicz and Dörnbrack (2008) underlined that the Durran system retains the full momentum equation and, consequently, admits unabbreviated baroclinic production of vorticity, as also observed by Klein (2009a). Achatz et al. (2010) demonstrated a multi-scale asymptotic consistency between the pseudo-incompressible system and the compressible Euler equations to leading order, which cannot be observed for the anelastic system.

The pseudo-incompressible equations are thus suitable for studying full scale gravity-wave dynamics from their generation until their breaking. In this problem the distances covered by waves of interest, both in the horizontal and in the vertical, are typically far too large to allow an explicit direct simulation of the generated turbulence. For its parameterization an implicit large-eddy-simulation (ILES) method as developed by Adams et al. (2004) and Hickel et al. (2006, 2007) seems attractive. This so called adaptive local deconvolution method (ALDM) represents a merger of numerical method and SGS turbulence parameterization. Instead of keeping numerical truncation errors small, which can be quite costly or unfeasible, and later dissipate the solution with an explicit turbulence model, numerical truncation is deliberately exploited and tuned to act as turbulence model. This holistic approach results in a particularly reliable and efficient method, while turbulence spectra are matched well. ALDM has been calibrated to be consistent with EDQNM spectral turbulence theory (Hickel et al. 2006). Indeed, comparisons with direct numerical simulation (DNS) data of turbulent flows showed better spectral behavior than standard turbulence models. ALDM was originally developed for incompressible flows (Hickel et al. 2006, 2007) and subsequently extended to fully compressible turbulence (Hickel 2011; Hickel and Larsson 2008). Although its already wide-spread application in engineering applications (Klar et al. 2011; Hickel et al. 2011) had been limited to the description of the effects of unstratified turbulence, recent results by Remmler and Hickel (2012a,b) demonstrate that the method can also be applied to stratified turbulence governed by the Boussinesq equations. Here we report the first application of ALDM to full-scale atmospheric flows beyond the Boussinesq

approximation.

For this purpose a novel fully conservative discretization method for Durran's pseudo-incompressible system has been developed, as previously achieved, to the best of our knowledge, only by Smolarkiewicz and Dörnbrack (2008) and Smolarkiewicz and Szmelter (2011). As the implicit turbulence model of ALDM is fully merged with the spatial discretization, an extension to another system of partial differential equations can be challenging. This paper shows how these challenges have been resolved within the framework of our newly developed atmospheric flow solver pincFloit (Pseudo-INCompressible FLow solver with Implicit Turbulence model). We emphasize that many numerical issues discussed here, such as the convergence criterion for the pseudo-incompressible equations and a divergence correction for reducing the number of Poisson-solver iterations, are relevant to any kind of finite-volume method.

The paper is organized as follows. In Sec. 1 we recall the pseudo-incompressible equations and present them in a conservative and scaled form suitable for the discretization by a conservative finite-volume model. The general approach to the discretization is given in Sec. 2. Some special issues concerning pitfalls in the application of conservative finite volume methods to stratified fluids with the pseudo-incompressible divergence constraint are discussed in Sec. 3. Numerical test cases in Sec. 4 close the text, while Sec. 5 gives a summary and conclusions.

a. Governing equations

The pseudo-incompressible equations were first derived by Durran (1989). If we restrict ourselves to adiabatic non-rotating dynamics, then the Durran system in conservative flux

form reads

$$(\rho\mathbf{u})_t + \nabla\cdot(\rho\mathbf{u}\mathbf{u}) + \frac{1}{\mathrm{Ma}^2}\frac{1}{\kappa}\bar{P}\nabla\pi' = -\frac{1}{\mathrm{Fr}^2}\rho'\mathbf{k} + \frac{1}{\mathrm{Re}}\nabla\cdot\Pi \tag{1}$$

$$\rho_t + \nabla\cdot(\rho\mathbf{u}) = 0 \tag{2}$$

$$\nabla\cdot(\bar{P}\mathbf{u}) = 0\,, \tag{3}$$

with the Mach number Ma, the Froude number[1] Fr and the Reynolds number Re, the velocity $\mathbf{u} = (u, v, w)$ with its zonal, meridional and vertical components, respectively, the potential temperature θ and the pseudo-incompressible (effective) density ρ. Further quantities are the Exner pressure

$$\pi = \left(\frac{p}{p_0}\right)^{\kappa} \tag{4}$$

with $\kappa = R/c_p$, where c_p is the specific heat at constant pressure and R is the specific gas constant of air, a constant reference pressure p_0 and the pressure p. Following the notation of Klein (2009b), we introduce $\bar{P}$ defined by

$$c_p\rho\theta = \frac{1}{\kappa}p_0^{\kappa}\bar{p}^{1/\gamma} =: \frac{1}{\kappa}\bar{P} \tag{5}$$

with the ratio of specific heats $\gamma = c_p/c_V$ set to 1.4 in all our calculations. The pseudo-incompressible (effective) density is defined through the equation of state

$$\bar{\pi} = \left(\frac{R}{p_0}\rho\theta\right)^{\gamma-1}\,. \tag{6}$$

This effective density is only coupled to the potential temperature and no longer to the (total) Exner pressure, which was replaced by the background-state Exner pressure $\bar{\pi}$ in the equation of state. Through this approximation the system of equations becomes sound proof. Since the background state – given by $(\bar{\rho}, \bar{\theta}, \bar{\pi})$ – satisfies the equation of state, the pseudo-incompressible (effective) density[2] satisfies

$$\rho\theta = \bar{\rho}\bar{\theta}\,. \tag{7}$$

[1]Please note that in the present paper the Froude number is defined as follows: $\mathrm{Fr} = u_{\mathrm{ref}}/\sqrt{g l_{\mathrm{ref}}}$ with reference velocity u_{ref} and reference length l_{ref}.

[2]In the following we only use the term "density" but always refer to the pseudo-incompressible (effective) density.

For better numerical accuracy and to avoid the well-balancing problem it is sensible to work with the fluctuation quantities for Exner pressure $\pi' = \pi - \bar{\pi}(z)$ and potential temperature $\theta' = \theta - \bar{\theta}(z)$.

The viscous stress tensor Π is given by

$$\Pi_{ij} = \eta \left(\frac{\partial u_i}{\partial x_j} + \frac{\partial u_j}{\partial x_i} - \frac{2}{3}\delta_{ij}\frac{\partial u_k}{\partial x_k} \right) \tag{8}$$

with the Kronecker symbol δ_{ij} and the dynamic shear viscosity coefficient η. The effect of volume viscosity is not considered. Note, that the viscosity term is responsible for the *resolved grid scale dissipation* and is part of the model even if an implicit LES is used since the latter treats the *subgrid-scale dissipation*.

b. Transport of potential temperature

Substituting the density of the thermodynamic relation (5) into the effective continuity equation (2) and using the divergence constraint (3) we obtain a thermodynamic equation for the transport of potential temperature

$$(1/\theta)_t + \mathbf{u} \cdot \nabla(1/\theta) = 0 \,, \tag{9}$$

which is equivalent to $\frac{\mathrm{D}1/\theta}{\mathrm{D}t} = \frac{\mathrm{D}\theta}{\mathrm{D}t} = 0$. This shows that without heat sources the potential temperature is simply advected with the flow. If we combine effective continuity equation (2) and transport of potential temperature (9) we obtain the relation

$$(\rho\theta)_t + \nabla \cdot (\rho\theta\mathbf{u}) = 0 \tag{10}$$

for the mass-weighted potential temperature. Using the divergence constraint $0 = \nabla\cdot(\bar{P}\mathbf{u}) = \nabla \cdot (\bar{\rho}\bar{\theta}\mathbf{u}) = \nabla \cdot (\rho\theta\mathbf{u})$ we see that $\rho\theta$ is constant in time. Note that for diabatic flows a heat source enters the RHS of the divergence constraint and the transport equation of the potential temperature.

2. Discretisation with ILES

We present the implicit LES proposed by Hickel (2011); Hickel et al. (2006, 2007) and Hickel and Larsson (2008) named *adaptive local deconvolution method* (ALDM). Originally introduced for incompressible and fully compressible flows, we adopt the approach to the pseudo-incompressible equations. We present general ideas in the main part and put some of the more technical aspects into the appendix.

a. General setup

All variables are stored in a C-grid fashion. Fig. 1 shows a finite volume cell of the density with the velocities defined at the cell interfaces. Each momentum component has its own cell shifted with respect to the mass cell by half a cell in the corresponding direction. To calculate the fluxes across the cell surfaces, point values of velocity and scalars are reconstructed there. To denote the reconstructed value at the right wall of cell ijk we use the symbol $\tilde{\phi}^R_{i,j,k}$ and the superscripts L, F, B, U, D for reconstruction to the left, forward, backward, upward and downward cell interface, respectively, please see also Fig. 2. The equations for these reconstructions terms are given in the appendix.

b. Adaptive deconvolution (reconstruction)

To obtain the values at the cell interface, ideas from numerical gas dynamics are borrowed and extended. In the weighted essentially non-oscillatory (WENO) method (Shu 1997) data within a cell is reconstructed using the cell-averages from neighbouring cells as depicted in Fig. 3 on the example of a fifth order WENO scheme with third order reconstruction polynomials. Note that the parabolas do not interpolate the data points since they are finite-volume cell averages and not finite-difference point values. At the cell interface $x_{i+1/2}$ three reconstructed values exist from the three stencils. In WENO the reconstructed values are averaged using solution adaptive weights. These weights are chosen in such a way that

the order of accuracy in smooth flows approaches the maximum for the given stencil width while unphysical oscillations are avoided by keeping the total variation in non-smooth regions bounded.

ALDM differs from WENO in two ways. First, with ALDM the weights in the convex combination of the reconstruction polynomials are used to optimize the nonlinear spectral numerical dissipation that acts as an implicit SGS model rather than maximizing the formal order of accuracy. Second, in contrast to WENO, where polynomials of a certain degree n are used to obtain a convergence order $2n-1$, in ALDM first, second and third-order reconstructions are blended. The blending weights, again, are degrees of freedom that are used for SGS model tuning. For more details please see the appendix or Hickel et al. (2006, 2007).

c. Numerical flux function

To calculate the update of a quantity in cell (i,j,k) we need to discretize the divergence operator, which is done in a conservative finite-volume way:

$$\nabla \cdot F = \frac{f_{i+1/2,j,k} - f_{i-1/2,j,k}}{\Delta x} + \frac{g_{i,j+1/2,k} - g_{i,j-1/2,k}}{\Delta y} + \frac{h_{i,j,k+1/2} - h_{i,j,k-1/2}}{\Delta z} \,, \qquad (11)$$

where f, g and h indicate the fluxes in the three spatial directions as depicted in Fig. 4 for the flux of zonal momentum. The numerical flux function $f_{i+1/2,j,k}$ is the second ingredient of ALDM for ILES. It consists of a central term of high order and an artificial viscosity term. Mass and momentum have slightly different flux functions.

1) Mass flux function

For scalar transport it was shown in (Hickel et al. 2007) that the following flux function leads to an implicit SGS model that is consistent with turbulence theoretical constraints:

$$f^{\rho}_{i+1/2,j,k} = \frac{\tilde{\rho}^{R}_{i,j,k} + \tilde{\rho}^{L}_{i+1,j,k}}{2} u_{i,j,k} - \sigma_{i+1/2,j,k}(\tilde{\rho}^{L}_{i+1,j,k} - \tilde{\rho}^{R}_{i,j,k}) \,, \qquad (12)$$

where

$$\sigma_{i+1/2,j,k} = \sigma_C |\tilde{u}^R_{i,j,k} - \tilde{u}^L_{i,j,k}| \ . \tag{13}$$

The first part of the flux function leads to a high order central difference. Here it is important to work with the filtered (cell-centred, volume-averaged) velocity u, which satisfies the pseudo-incompressible divergence constraint. The second term is a dissipative term, with a diffusion coefficient given in (13), which itself depends on the roughness of the velocity field and a tuning parameter σ_C. In a smooth velocity field a density distribution is (almost) not diffused numerically with this SGS ansatz. Throughout our calculations we use for the tuning parameter

$$\sigma_C = 0.615 \tag{14}$$

as proposed in (Hickel et al. 2007) for air.

2) Momentum flux function

The location of the fluxes on a C-grid is depicted in Fig. 4. To show the principle of the numerical flux function for the momentum we give the meridional transport of zonal momentum

$$g^{\rho u}_{i,j+1/2,k} = \hat{\rho}_{i+1/2,j+1/2,k} \left\{ \frac{1}{4} (\tilde{u}^F_{i,j,k} + \tilde{u}^B_{i,j+1,k})(\tilde{v}^R_{i,j,k} + \tilde{v}^L_{i+1,j,k}) - \sigma^{\mathbf{u}}_{i,j+1/2,k} (\tilde{u}^B_{i,j+1,k} - \tilde{u}^F_{i,j,k}) \right\} \ , \tag{15}$$

where

$$\sigma^{\mathbf{u}}_{i,j+1/2,k} = \sigma^{\mathbf{u}} \, |u_{i,j,k} - u_{i,j+1,k}| \ . \tag{16}$$

At first we note that all quantities used in (15) are reconstructed to the forward interface centre of the momentum cell of $\rho u_{i,j,k}$. The interpolation of the density $\hat{\rho}_{i+1/2,j+1/2,k}$ is – at first glance – not unique but it can be constrained so as to make momentum and effective continuity equation consistent – an aspect discussed in Sec. 3 a. The first part of the flux function (15) is a central interpolation leading to a high-order central difference for the divergence operator. The second term is a numerical diffusion term that dissipates momentum

according to the magnitude of the second derivative of the reconstructed (deconvolved in LES terms) velocity $\tilde{u}$. The SGS dissipation coefficient $\sigma^{\mathbf{u}}_{i,j+1/2,k}$ given in (16) is proportional to the roughness of the volume-averaged (filtered in LES terms) velocity u. A list of all flux components can be found in the Appendix a. Also note that $\sigma^{\mathbf{u}}$ depends on the location if the grid is not uniform, i. e. with varying mesh size (Hickel et al. 2006). In pincFloit a uniform Cartesian mesh is used so that this parameter is a constant

$$\sigma^{\mathbf{u}} = 0.06891\ . \tag{17}$$

3. Numerical Issues

The implicit LES was devised for incompressible flows by Hickel et al. (2006) and for fully compressible flows by Hickel and Larsson (2008) and Hickel (2011). The application of ALDM to a model with atmospheric background stratification and a background density rapidly decaying in the vertical lead to a number of problems – the solution of which we discuss in this section.

a. Flux function: Consistency between continuity and momentum equation

So far we have not devised a rule how to interpolate the densities $\hat{\rho}$ needed in the momentum fluxes. We require that a pure density distribution with homogeneous background wind should solely advect the density while maintaining the constant background wind for all times. This goal can be achieved by assuring that effective continuity and momentum equation do – in this special setting – exactly the same, namely pure transport of mass. Note that inconsistent interpolation of $\hat{\rho}$ leads to the appearance of artificial velocity fluctuations.

For simplicity, we assume at first a constant wind in zonal direction. We list all assumptions for the state at time $t = t_n$:

$$\rho = \rho(\mathbf{x}, t), \qquad u_i = u = \text{const}, \quad v = w = 0, \qquad \pi = \text{const}\ .$$

The following discussion applies most directly to multistage time-stepping schemes, such as Runge-Kutta, which can be seen as a series of appropriately weighted forward Euler steps, here called predictor step. With only zonal transport of momentum the equation for velocity predictor u_i^* reads:

$$\begin{aligned}\rho_{i+1/2}^{n+1} u_i^* &= \rho_{i+1/2}^n u_i^n - \Delta t \frac{f_{i+1/2}^{\rho u} - f_{i-1/2}^{\rho u}}{\Delta x} \\ &= \rho_{i+1/2}^n u_i^n - \frac{\Delta t}{\Delta x}\left[\frac{1}{4}\hat{\rho}_{i+1}^n (\tilde{u}_{i+1}^L + \tilde{u}_i^R)^2 - \frac{1}{4}\hat{\rho}_i^n (\tilde{u}_i^L + \tilde{u}_{i-1}^R)^2\right] .\end{aligned}$$

For ease of reading we omitted the spatial indices j and k. The density at the zonal-velocity position is taken to be $\rho_{i+1/2} = (\rho_i + \rho_{i+1})/2$. Note that for constant u the correction term containing σ is absent. The position of density, velocity and fluxes can be seen in Fig. 5.

We now enforce

$$u_i^* = u_i^n = u ,$$

i. e. no change of velocity in time, apply the assumption $u_i = u = \text{const}$ and obtain

$$\frac{\rho_{i+1/2}^{n+1} - \rho_{i+1/2}^n}{\Delta t} u = -\frac{1}{\Delta x}(\hat{\rho}_{i+1}^n u^2 - \hat{\rho}_i^n u^2) \tag{18}$$

for the *momentum equation*. With the same assumptions, the continuity equation for cell i reads

$$\begin{aligned}\frac{\rho_i^{n+1} - \rho_i^n}{\Delta t} &= -\frac{f_{i+1/2}^{\rho} - f_{i-1/2}^{\rho}}{\Delta x} \\ &= -\frac{1}{\Delta x}\left[\frac{\tilde{\rho}_i^R + \tilde{\rho}_{i+1}^L}{2} u - \frac{\tilde{\rho}_{i-1}^R + \tilde{\rho}_i^L}{2} u\right]\end{aligned}$$

and for cell $i+1$

$$\frac{\rho_{i+1}^{n+1} - \rho_{i+1}^n}{\Delta t} = -\frac{1}{\Delta x}\left[\frac{\tilde{\rho}_{i+1}^R + \tilde{\rho}_{i+2}^L}{2} u - \frac{\tilde{\rho}_i^R + \tilde{\rho}_{i+1}^L}{2} u\right] .$$

The arithmetic mean of both continuity equations yields

$$\frac{\rho_{i+1/2}^{n+1} - \rho_{i+1/2}^n}{\Delta t} = -\frac{1}{\Delta x}\left[\frac{\tilde{\rho}_{i+1}^R + \tilde{\rho}_{i+2}^L}{4} u - \frac{\tilde{\rho}_{i-1}^R + \tilde{\rho}_i^L}{4} u\right] . \tag{19}$$

Note that this arithmetic averaging agrees with the interpolation

$$\rho_{i+1/2,j,k} = \frac{1}{2}(\rho_{i,j,k} + \rho_{i+1,j,k}) \tag{20}$$

used to obtain the density for the momentum $\rho_{i+1/2,j,k}u_{i,j,k}$. We now require that momentum transport (18) and mass transport (19) are equal:

$$\hat{\rho}^n_{i+1} - \hat{\rho}^n_i = \frac{\tilde{\rho}^R_{i+1} + \tilde{\rho}^L_{i+2}}{4} - \frac{\tilde{\rho}^R_{i-1} + \tilde{\rho}^L_i}{4} \ .$$

The two differences are depicted in Fig. 6. It can easily be checked that this equality is obtained if the density $\hat{\rho}$ is interpolated like

$$\hat{\rho}^n_{i+1,j,k} = \frac{1}{4}(\tilde{\rho}^R_{i,j,k} + \tilde{\rho}^L_{i+1,j,k} + \tilde{\rho}^R_{i+1,j,k} + \tilde{\rho}^L_{i+2,j,k}) \ , \tag{21}$$

where we have added the two missing indices j and k for completeness. This interpolation rule, which is the only possible solution of the form $\hat{\rho}^n_{i+1} = \sum_{j=-\infty}^{\infty} a_j\tilde{\rho}^R_{i+j} + b_j\tilde{\rho}^L_{i+1+j}$ with $a_{-\infty} = b_{-\infty} = a_\infty = b_\infty = 0$, is illustrated in Fig. 7. This reasoning can be generalised to 3D. A list of all interpolation rules can be found in the Appendix b.

b. Temporal discretisation

1) Choosing the time step

PincFloit can be run with a *fixed* time step or with a *variable* time step chosen according to several stability criteria to obtain an efficient and stable numerical model. The stability criterion by Courant, Friedrichs and Levy limits the time step in proportion to the grid-point spacing but inversely proportional to the advecting wind speed. We thus choose the time step in the following way for our model

$$dt_{\mathrm{CFL}} = \nu \min(\frac{\Delta x}{|u_{\max}|}, \frac{\Delta y}{|v_{\max}|}, \frac{\Delta z}{|w_{\max}|}) \ . \tag{22}$$

The CFL number ν is set to 0.9 in most of the calculations in conjunction with 3rd-order Runge-Kutta schemes.

The CFL condition for a thermal bubble – initially at rest in a windless atmosphere – would allow an infinitely large first time step. Therefore the *acceleration a* must be considered

as well (Remmler 2010)

$$\frac{1}{2}\left|a\right|\Delta t^2 + \left|u\right|\Delta t = \nu \Delta x \quad \text{with} \quad \nu \leq 1\ . \tag{23}$$

Solving for the positive root of Δt leads to

$$\Delta t = -\frac{|u|}{|a|} + \sqrt{\frac{|u|^2}{|a|^2} + \frac{2\nu\Delta x}{|a|}}\ . \tag{24}$$

To avoid division by zero, we follow the algorithm – here in 1D: First obtain $u_{\max} = \max|u|$ and $a_{\max} = \max|a|$, then calculate the time step according to the standard CFL condition $\Delta t_{\mathrm{CFL}} = \min(\nu\Delta x/\left|u\right|, \Delta t_{max})$ and if the speed up $\Delta u = a_{\max}\Delta t_{\mathrm{CFL}}$ is essential, i. e. if $\Delta u > \varepsilon u_{\max}$ with e. g. $\varepsilon = 10^{-2}$, then compute

$$\Delta t_{\mathrm{Buoy}} = -\frac{u_{\max}}{a_{\max}} + \sqrt{\frac{u_{\max}^2}{a_{\max}^2} + \frac{2\nu\Delta x}{a_{\max}}}\ . \tag{25}$$

We want to resolve the oscillations related to *gravity waves (GW)* in time. The highest possible GW frequency is the Brunt-Väisälä frequency N. A sensible time step limit is therefore given by $\Delta t_{GW} = 1/N$. For our standard GWP test case with an isothermal background of $T = 300$ K and $N = 0.018s^{-1}$ we obtain a time step limitation due to gravity wave oscillations of $\Delta t_{GW} = 55$ s. The time step to be used by the scheme is the minimum of the time steps dictated by the various time step restrictions and a $\Delta t_{\max}$ to avoid too large numerical errors.

2) Low-Storage Runge-Kutta and Divergence Constraint

We have implemented (among other time schemes) the low storage Runge-Kutta method of third order by Williamson (1980)

$$q_1 = \Delta t F(\phi^n), \qquad \phi_1 = \phi^n + q_1/3, \tag{26}$$

$$q_2 = \Delta t F(\phi_1) - 5q_1/9, \qquad \phi_2 = \phi_1 + 15q_2/16, \tag{27}$$

$$q_3 = \Delta t F(\phi_2) - 153q_2/128, \qquad \phi^{n+1} = \phi_2 + 8q_3/15. \tag{28}$$

We derive the pressure correction procedure applied within each Runge-Kutta stage and show how this additional projection step changes the convergence properties of the overall scheme.

Without heat source, the divergence constraint on the velocity

$$\nabla \cdot \bar{P}\mathbf{u} = 0 \tag{29}$$

can be ensured by correcting the velocity field after the predictor step. Care has to be taken because this pressure correction has to be applied within each Runge-Kutta stage m. The equation for the tendency and the predictor of the momentum are given by:

$$\begin{aligned}
\Delta(\rho u)_i^* &= \Delta t F^m - \Delta t \frac{1}{\mathrm{Ma}^2}\frac{1}{\kappa}\bar{P}\frac{\delta \pi'^m}{\delta x_i} + \alpha^m \Delta(\rho u)_i^m && (30)\\
\rho^{m+1} u_i^* &= (\rho u)_i^m + \beta^m \Delta(\rho u)_i^* && (31)\\
&= (\rho u)_i^m + \beta^m \Delta t F^m - \beta^m \Delta t \frac{1}{\mathrm{Ma}^2}\frac{1}{\kappa}\bar{P}\frac{\delta \pi'^m}{\delta x_i} + \beta^m \alpha^m \Delta(\rho u)_i^m \ , && (32)
\end{aligned}$$

where u_i denotes a velocity component and ρ^{m+1} is known from the update of the effective continuity equation, F^M comprises all fluxes, forces and sources except for the pressure gradient and α^m, β^m are the weights for the low-storage Runge-Kutta method by Williamson (1980). The old pressure π'^m does not guarantee the divergence constraint on $\mathbf{u}^*$. Therefore a new pressure π'^{m+1} is sought which ensures that the velocity u_i^{m+1} at the next Runge-Kutta stage satisfies (29)

$$(\rho u)_i^{m+1} = \cdots\cdots\cdots\cdots\cdots - \beta^m \Delta t \frac{1}{\mathrm{Ma}^2}\frac{1}{\kappa}\bar{P}\frac{\delta \pi'^{m+1}}{\delta x_i} \cdots\cdots\cdots\cdots\cdots \ . \tag{33}$$

Taking the difference between the last two equations (32) and (33) and applying the discrete divergence operator $\delta/\delta x_i$ we obtain for the corrector procedure:

$$\begin{aligned}
\rho^{m+1}(u_i^* - u_i^{m+1}) &= \beta^m \Delta t \frac{1}{\mathrm{Ma}^2}\frac{1}{\kappa}\bar{P}\frac{\delta(\pi'^{m+1} - \pi'^m)}{\delta x_i} && (34)\\
\mathrm{Ma}^2\kappa \ \frac{\delta}{\delta x_i}\bar{P}u_i^* &= \beta^m \Delta t \frac{\delta}{\delta x_i}\left\{\frac{\bar{P}^2}{\rho^{m+1}}\frac{\delta}{\delta x_i}\Delta\pi'\right\} \qquad \longrightarrow \qquad \Delta\pi' && (35)\\
\pi'^{m+1} &= \pi'^m + \Delta\pi' && (36)\\
u_i^{m+1} &= u_i^* - \beta^m \Delta t \frac{1}{\mathrm{Ma}^2}\frac{1}{\kappa}\frac{\bar{P}}{\rho^{m+1}}\frac{\delta \Delta\pi'}{\delta x_i} \ , &&
\end{aligned}$$

where in the second line we sum over double indices giving the discrete divergence operator on the LHS and a Laplacian on the RHS.

Equation (35) is a *discrete Poisson equation* for the pressure correction $\Delta\pi'$ with the right hand side given as the residual divergence of the predicted velocity field $\mathbf{u}^*$ weighted with $\bar{P}$. Note that the predicted tendency Δu^* must also be corrected because it is used in the following Runge Kutta stage, i. e. we have to supplement the equation

$$\Delta u_i^{m+1} = \Delta u_i^* + \frac{\delta u_i}{\beta^m} \tag{37}$$

with $\delta u_i = u_i^{m+1} - u_i^*$. Alternatively to the correction of velocity, the momentum tendency could be corrected

$$\Delta(\rho\mathbf{u})^{m+1} = \Delta(\rho u)^* + \rho^{m+1}\frac{\delta\mathbf{u}}{\beta^m} \ . \tag{38}$$

It is known, that a fractional step method deteriorates the temporal convergence order of the overall numerical scheme. To quantify this error we tested three third-order Runge Kutta schemes with the 1D gravity wave packet test case: the low-storage Runge Kutta by Williamson (1980) (LS-Will-RK3), a low-storage TVD Runge Kutta (LS-TVD-RK3) and a classical, non low-storage TVD Runge Kutta scheme (CL-TVD-RK3) (Gottlieb and Shu 1998). The results are presented in Fig. 8. If the projection step is switched off all third-order schemes show the expected third-order convergence as $\Delta t \to 0$. If the projection is switched on the convergence drops down to first order as a simple forward Euler. Note, however, that the overall error of the third-order schemes is one order of magnitude smaller so that it pays off to work with the higher-order schemes.

c. ALDM with background stratification

It turned out that the turbulence model should not be applied to the full density but only to the perturbations. Otherwise the model would "see" roughness in the background, which it would try to smooth out, i. e. it would try to establish a linear background profile. This can

also be seen on the equation level: since the divergence in the effective continuity equation (2) must be discretized with the ALDM flux function it cannot be consistent with the divergence constraint (3). We consider an unperturbed isentropic background, for simplicity, so that the divergence constraint becomes

$$\bar{\theta} = \text{const} \Rightarrow \nabla \cdot (\bar{\rho}\bar{\theta}\mathbf{u}) = \nabla \cdot (\bar{\rho}\mathbf{u}) = 0 \tag{39}$$

and the effective continuity equation with $\rho = \bar{\rho}$ simplifies to

$$\rho_t + \nabla \cdot (\bar{\rho}\mathbf{u}) = 0 \Rightarrow \rho_t = 0 \; . \tag{40}$$

The straightforward discretisation of (2) does not satisfy (40). The discrete divergence

$$\hat{\nabla}\cdot(\tilde{\rho}\mathbf{u}) = \frac{h_{k+1/2} - h_{k-1/2}}{\Delta z} \tag{41}$$

with

$$h_{k+1/2} = \frac{\tilde{\rho}_k^U + \tilde{\rho}_{k+1}^D}{2}\bar{w}_k - \text{regularization term} \tag{42}$$

does not vanish because the background density has a non-trivial profile leading to reconstruction values that no longer satisfy the divergence constraint

$$\tilde{\rho} = \tilde{\bar{\rho}}(z) \neq \bar{\rho}(z) \Rightarrow \hat{\nabla}\cdot(\tilde{\rho}\mathbf{u}) \neq 0 \Rightarrow \rho_t \neq 0 \; . \tag{43}$$

A simple way out is to split the total density into the background $\bar{\rho}$ and a fluctuation part ρ' and apply the reconstruction only to ρ'. The ILES damping term in the flux will only depend on $\tilde{\rho}'$, while the density in the convective term will be composed of background and reconstructed fluctuation:

$$\rho = \bar{\rho} + \rho' \Rightarrow \tilde{\rho}_{conv} = \bar{\rho} + \tilde{\rho}' \text{ and } \tilde{\rho}_{ILES} = \tilde{\rho}' \; . \tag{44}$$

The flux in the above situation takes the form

$$h_{k+1/2} = \frac{\bar{\rho}_k + \bar{\rho}_{k+1}}{2}\bar{w}_k - 0 = \bar{\rho}_{k+1/2}\bar{w}_k \; , \tag{45}$$

which leads to

$$\hat{\nabla}\cdot(\tilde{\rho}\mathbf{u}) = \hat{\nabla}\cdot(\bar{\rho}\mathbf{u}) = 0 \Rightarrow \rho_t = 0 \; . \tag{46}$$

Accordingly, the flux function (12) is replaced by

$$f^{\rho}_{i+1/2,j,k} = \frac{(\bar{\rho}_{i,j,k} + \tilde{\rho}'^{R}_{i,j,k}) + (\bar{\rho}_{i,j,k} + \tilde{\rho}'^{L}_{i+1,j,k})}{2} u_{i,j,k} - \sigma_{i+1/2,j,k}(\tilde{\rho}'^{L}_{i+1,j,k} - \tilde{\rho}'^{R}_{i,j,k}) \; . \tag{47}$$

In Fig. 9 the effect of introducing the fluctuation density is shown with isolines of potential temperature for the hot bubble test case at $t = 20$ min (see Sec. 4 for the set up). On the left the discretisation with the total density leads to oscillations in the solution, while the introduction of density fluctuation (right) produces a smooth solution. The small scale structures on the left are on the grid scale and are numerical artefacts. Especially the oscillations at the top of the domain are unphysical since the solution should remain smooth away from the bubble induced vortices. The smooth solution on the right compares well with other simulations of the test case in the literature, e. g. Robert (1993); Klein (2009a); Mendez-Nunez and Carroll (1994).

A similar positive effect can be observed for the 1D gravity wave packet (see Sec. 4 for the set up) shown in Fig. 10. If the total density is reconstructed, severe oscillations appear in the solution (left). ALDM applied only to the density fluctuations leads to a smooth solution (right), which is the correct solution since the gravity wave should not break and produce turbulence in this regime.

d. Solving the Poisson problem

Throughout our calculations we use the BICGSTAB (Meister 1999) algorithm to solve the Poisson problem. A small parameter ε is introduced in the abort criterion, which will be discussed in Sec. 2.

1) Scaling of the Poisson equation

If we solve the Poisson equation to satisfy $\|\nabla \cdot (\bar{P}\mathbf{u})\| \leq \varepsilon$, we obtain a height-dependent error in the velocity since $\bar{\rho}\bar{\theta}$ depends exponentially on height. In Fig. 11 this is shown for a (initially) uniform, isothermal atmosphere at rest with a domain ranging up to $z_{\max} = 150$ km with a Poisson solver tolerance of $\varepsilon = 10^{-7}$ and a fixed time step of one second. One way out of this would be to tighten the tolerance – a very inefficient way. We consider a different approach: scaling of the Poisson equation. To see the necessity we analyse the problem by looking at the influence of the divergence error on the effective continuity equation and, consequently, via the momentum equation on the velocity field.

The effective continuity equation $\rho_t + \nabla \cdot (\rho \mathbf{u}) = 0$ with the density split as $\rho = \bar{\rho} + \rho'$ reads

$$\rho'_t + \nabla \cdot (\bar{\rho}\mathbf{u}) + \nabla \cdot (\rho' \mathbf{u}) = 0 \, . \tag{48}$$

The second term is related to the divergence constraint in the following way. Assuming a Poisson solver tolerance of ε and using $\bar{P} = \bar{\rho}\bar{\theta}$, then

$$\|\nabla \cdot (\bar{\rho}\bar{\theta}\mathbf{u})\| \sim \|\bar{\theta}\nabla \cdot (\bar{\rho}\mathbf{u})\| + \|\bar{\rho}\mathbf{u} \cdot \nabla\bar{\theta}\| \sim \varepsilon \tag{49}$$

and consequently

$$\|\nabla \cdot (\bar{\rho}\mathbf{u})\| \sim \|\frac{1}{\bar{\theta}} \underbrace{\nabla \cdot (\bar{\rho}\bar{\theta}\mathbf{u})}_{\sim\varepsilon}\| - \|\bar{\rho}\mathbf{u} \cdot \nabla \ln\bar{\theta}\| \, . \tag{50}$$

The divergence error in the density therefore has the following height dependency, assuming the second term of the RHS of (50) to be negligible in this order estimate,

$$\|\rho'_{div\ error}\| \sim \frac{1}{\|\bar{\theta}\|}\varepsilon \, . \tag{51}$$

An error in the density leads to a buoyant acceleration in the vertical momentum equation

$$\|(\rho w')_t\| \sim \|\rho'_{div\ error} g\| \tag{52}$$

$$\|(\bar{\rho} w')_t\| \sim \|\rho'_{div\ error} g\| \quad \text{assuming} \quad \|\rho'_{div\ error}\| \ll \|\bar{\rho}\| \tag{53}$$

$$\|w'_t\| \sim \|\frac{\rho'_{div\ error}}{\bar{\rho}} g\| \tag{54}$$

$$\|w'_t\| \sim \frac{\varepsilon}{\|\bar{\rho}\bar{\theta}\|} g \ , \tag{55}$$

where we used relation (51) for the last step. Now it is obvious that the velocity perturbation w' created due to the divergence error is height dependent and will grow exponentially like $(\bar{\rho}\bar{\theta})^{-1}$.

To obtain height-independency for w' we see from (54) that the divergence error in the density should scale as

$$\|\rho'_{div\ error}\| \sim \|\bar{\rho}\| \varepsilon \ . \tag{56}$$

Then the divergence error in the effective continuity equation, i. e. first term of the RHS of (50), should satisfy

$$\|\frac{1}{\bar{\theta}} \nabla \cdot (\bar{\rho}\bar{\theta}\mathbf{u})\| \sim \|\bar{\rho}\| \varepsilon \ , \tag{57}$$

which is equivalent to the following scaling of the divergence constraint

$$\|\frac{1}{\bar{\rho}\bar{\theta}} \nabla \cdot (\bar{\rho}\bar{\theta}\mathbf{u})\| \sim \varepsilon \ . \tag{58}$$

If we apply this pressure scaling ($\bar{\rho}\bar{\theta} = \bar{P}$) while keeping the Poisson solver tolerance at $\varepsilon = 10^{-7}$ we obtain the results presented in Fig. 12. With the same computational effort velocity and potential temperature perturbations were reduced by four orders of magnitude. Note, for the anelastic divergence constraint a scaling with $\bar{\rho}$ would be in order.

2) Physical convergence criterion

Smolarkiewicz et al. (1997) discussed stopping criteria for the iterative solution of the Poisson problem in the context of the Boussinesq system. Their main argument is a physical

one: an iteration should be stopped, if the relative density change $\Delta\rho/\rho$ due to the divergence error within one time step Δt is smaller than some ε. A convergence to machine precision would be a waste of time since other discretisation errors are then orders of magnitudes larger.

Here we discuss it in the context of the pseudo-incompressible system. From (48) and (50) we recall that the divergence constraint enters the effective continuity equation in the form

$$\rho_t + \frac{1}{\bar{\theta}}\nabla\cdot(\bar{\rho}\bar{\theta}\mathbf{u}) - \ldots = 0\ . \tag{59}$$

The density change due to the divergence error in one time step is

$$\frac{\Delta\rho_{div\ error}}{\Delta t} \sim \frac{1}{\bar{\theta}}\nabla\cdot(\bar{\rho}\bar{\theta}\mathbf{u}) \tag{60}$$

and the relative change with respect to the background density is

$$\frac{\Delta\rho_{div\ error}}{\bar{\rho}} \sim \Delta t\frac{1}{\bar{\rho}\bar{\theta}}\nabla\cdot(\bar{\rho}\bar{\theta}\mathbf{u})\ . \tag{61}$$

To ensure that the relative change of density is small throughout the computational domain a sensible abort criterion is

$$\|\Delta t\frac{1}{\bar{\rho}\bar{\theta}}\nabla\cdot(\bar{\rho}\bar{\theta}\mathbf{u})\|_\infty \leq \varepsilon\ . \tag{62}$$

Note that the scaling of the divergence is consistent with the scaling we introduced in the section above. This is because we also assume in both cases that density errors are proportional to the background density.

3) Correcting the divergence error

Smolarkiewicz and Margolin (1994) showed that there can be an enormous difference between the Eulerian and the semi-Lagrangian approach: the flux-form formulation needs a much smaller Poisson solver tolerance ε in the iterative elliptic solver to avoid unphysical solutions than the advective formulation[3]. This leads to a higher number of iterations and

[3]It is also shown that this problem can be circumvented by transporting only the perturbation of the potential temperature instead of the full quantity.

increase in computing time. In our model we also observed this inefficiency of the Poisson solver and propose the following remedy, which, on the one hand, violates the conservation property of the effective continuity equation. On the other hand this error is of the order of the Poisson solver tolerance and is therefore acceptable – depending on the application.

To understand the modification let us write once more the effective continuity equation $\rho_t + \nabla \cdot (\rho \mathbf{u}) = 0$ in a different form

$$\rho_t + \underbrace{\frac{1}{\bar{\theta}} \nabla \cdot (\bar{\rho}\bar{\theta}\mathbf{u})}_{O(\varepsilon)} - \bar{\rho}\mathbf{u}\frac{\nabla \bar{\theta}}{\bar{\theta}} + \nabla \cdot (\rho' \mathbf{u}) = 0 \tag{63}$$

so that the term containing the divergence error becomes visible. If the tolerance ε is very small the term can be neglected in all other cases it has a (unphysical) effect. To overcome this discrepancy, we simply subtract this term from the equation, which is the same as adding it as a source term in the effective continuity equation:

$$\rho_t + \nabla \cdot (\rho \mathbf{u}) = \frac{1}{\bar{\theta}} \nabla \cdot (\bar{\rho}\bar{\theta}\mathbf{u}) \; . \tag{64}$$

In the following we study the effect of the proposed "divergence error correction" for the 1D gravity wave packet, which is a very sensitive test case. In Fig. 13 the 1D gravity wave packet described in Sec. 4 is shown. If the effective continuity equation is not changed (left column) we can see that for a Poisson solver tolerance of $\varepsilon = 10^{-5}$ (top) the scheme is not even stable and for $\varepsilon = 10^{-7}$ (bottom) there are oscillations in the higher altitude regions. In contrast, the introduction of the source term in the effective continuity equation stabilises the scheme and produces correct results for tolerances as low as $\varepsilon = 10^{-5}$. In table 1 we see how the average number of iterations per call to BICGSTAB[4], is reduced by introducing the divergence error correction. The reason for this behaviour is clear: if the error is not produced in the effective continuity equation, no unphysical dynamic is induced in the momentum equation – and an initially unperturbed, divergence-constraint satisfying state maintains this divergence constraint. Note that for $\varepsilon \leq 10^{-8}$ the divergence error

[4]Note that each iteration within BICGSTAB has two calls of the linear operator.

correction has no influence any more. Also note that in some instances BICGSTAB is not called at all leading to average numbers smaller than 1.

4. Test Case Results

a. Hot bubble test case

For the hot bubble test case described by Mendez-Nunez and Carroll (1994) we assume a neutrally stratified atmosphere with $\theta_{00} = 300$ K. The initial perturbation by the hot thermal is given by

$$\Delta\theta = \Delta\theta_0 \cos^2(\frac{\pi r}{2}) \quad \text{for} \quad r \leq 1 \tag{65}$$

with the radial distance given by

$$r^2 = \left(\frac{x - x_c}{r_0}\right)^2 + \left(\frac{z - z_c}{r_0}\right)^2 . \tag{66}$$

The radius is set to $r_0 = 2.5$ km and the initial height is $z_c = 2.75$ km. The bubble is placed horizontally in the middle of the domain. This test case was chosen to demonstrate the importance of transporting only the density perturbation instead of the full density, see Fig. 9 and the discussion in Sec. 3 c. The test shows interfacial instabilities as already reported in Grabowski and Clark (1991) for a thermal with moist physics and a high resolution (direct simulation) approach.

We now consider a variant of the hot bubble test case with a more realistic atmosphere. The troposphere is assumed isentropic with $\theta_{tr} = 300$ K, the tropopause is set at $z_{tr} = 12$ km and the stratosphere is assumed isothermal with a constant temperature given by the temperature at the tropopause

$$T_{tr} = \theta_{tr} \left(\frac{p_{tr}}{p_0}\right)^{R/c_p} , \tag{67}$$

with the pressure at the tropopause

$$p_{tr} = p_0 \big(1 - \frac{g z_{tr}}{c_p \theta_{tr}}\big)^{c_p/R} . \tag{68}$$

The potential temperature profile in the stratosphere is given by

$$\bar{\theta}(z) = \theta_{tr} \exp\left[\frac{g}{c_p T_{tr}}(z - z_{tr}\right] \ . \tag{69}$$

The result of the simulation with the implicit turbulence model at a resolution of 100×100 at 20 minutes model time is shown in Fig. 14. Depicted are the isolines of potential temperature perturbation $\theta' = \theta - \bar{\theta}$ ranging from -3.2 K to 2.2 K in steps of 0.5 K. Positive perturbations are marked with a "+" and negative perturbations with a "−". As for a convective cell in moist atmosphere, the tropopause acts as a natural border for the vertical movement of the hot bubble and its spreading looks similar to experiments with a solid wall at $z = z_{tr}$. Nevertheless, the updraft produced by the hot bubble induces perturbations at the tropopause, which travel as gravity waves into the stratosphere. Wave crests and troughs are visible in 14 as elliptic isolines with positive and negative values of potential temperature.

b. Bubble test case by Robert

Robert (1993) discussed the test case of two colliding bubbles: a large hot bubble with a small cold bubble placed horizontally off-centred above. The background is an isentropic atmosphere with $\bar{\theta} = 300$ K. Both bubbles have the following structure

$$\Delta\theta = \begin{cases} \Delta\theta_0, & r \le r_0 \\ \Delta\theta_0 \mathrm{e}^{-(r-r_0)^2/\sigma^2}, & r > r_0 \end{cases} \tag{70}$$

with

$$r^2 = (x - x_0)^2 + (z - z_0)^2 \ . \tag{71}$$

The warm bubble has the data $\Delta\theta_0 = 0.5$ K, $r_0 = 150$ m, $\sigma = 50$ m and is positioned at $x_0 = 500$ m, $z_0 = 300$ m. The smaller cold bubble has the data $\Delta\theta_0 = -0.15$ K, $r_0 = 0$ m, $\sigma = 50$ m and is positioned at $x_0 = 560$ m, $z_0 = 640$ m. The domain spans $[-500 \text{ m}, 500 \text{ m}] \times [0, 1000 \text{ m}]$. No-slip boundary conditions are applied at all four walls of the domain. The CFL number is set to 0.9 leading to a time step of 3.0 seconds for

100 × 100 and 1.5 seconds for the 200 × 200 resolution. An interesting aspect is the existence of two scales introduced by the large and small bubble and the fact that the cold bubble is horizontally "off-centred", which creates a highly unsymmetric solution. In Fig. 15 we compare the isolines of density perturbation $\rho' = \rho - \bar{\rho}$ after 10 minutes for two resolutions: 100 × 100 on the left column and 200 × 200 on the right. The solution for the Euler equations with an upwind scheme by Robert is presented in the top line of the figure, while the solution with pincFloit – i. e. for the *pseudo-incompressible equations* with ALDM as implicit turbulence model – is shown in the bottom line. The resemblance of the solutions is remarkable. A major difference is the vortex at the lower right corner: pincFloit produces more structure in this flow region. As it turns out this structure is also obtained with an upwind scheme (pincFloit with MUSCL as flux solver) for a higher resolution (400 × 400). This implies that ALDM has less numerical dissipation than standard (second-order) upwind schemes at a comparable resolution.

A variant of Robert's test case with a uniform horizontal background wind $u_0 = 1.67$ m s^{-1} is shown in Fig. 16 with a resolution of 200×200. The velocity is set so that the bubbles fully traverse the periodic domain within 10 minutes. The plotted levels for the isolines of density perturbation $\rho' = \rho - \bar{\rho}$ are the same for the experiment without background wind (left column) and with uniform background wind (right column). The results with and without wind are not identical but very close to each other. The small deviation can be attributed to numerical truncation errors, which are different if the fluid system is shifted along the grid and exponentially grow in time due to the non-linear transport processes.

c. 1D Gravity Wave Packet

On an isothermal reference state with $T_{00} = 300$ K a wave packet is superimposed with the initial buoyancy amplitude

$$\hat{b}(x,z) = a\frac{N^2}{m_0}\exp\left[\frac{(z-z_c)^2}{2\sigma^2}\right]\sqrt{\frac{\overline{\rho}(0)}{\overline{\rho}(z)}} \tag{72}$$

with the vertical wave number $m_0 = 2\pi/\lambda_{z,0}$ and the normalised amplitude $a = 0.1$, the isothermal Brunt-Väisälä frequency for $T_{00} = 300$ K of $N = 0.018$ s^{-1}, the half-width $\sigma = 5$ km and the centre of the wave packet at $z_c = 30$ km. Using the polarisation relations we set the following initial fields

$$u_{t=0} = \frac{m_0}{k_0}\frac{\hat{\omega}}{N^2}\hat{b}\cos(k_0 x + m_0 z - \frac{\pi}{2}) \tag{73}$$

$$w_{t=0} = \frac{\hat{\omega}}{N^2}\hat{b}\cos(k_0 x + m_0 z + \frac{\pi}{2}) \tag{74}$$

$$b_{t=0} = \hat{b}\cos(k_0 x + m_0 z) \tag{75}$$

$$\pi_{t=0} = \frac{m_0}{k_0^2}\frac{\hat{\omega}^2}{N^2}\frac{1}{c_p\theta_0(z)}\hat{b}\cos(k_0 x + m_0 z - \frac{\pi}{2})\ . \tag{76}$$

For the wave lengths we set $\lambda_x = \lambda_z = 1$ km defining the initial wave number $\mathbf{k}_0 = (k_0, m_0)$ and the intrinsic frequency $\hat{\omega} = -Nk_0/\|\mathbf{k}_0\|$. The domain of the full model has the size $(l_x, l_z) = (1\text{ km}, 60\text{ km})$ at a resolution of $n_x \times n_z = 64 \times 3840$. In both test cases the domain is periodic in the horizontal and has a no-slip solid wall boundary condition at the bottom and top. A sponge layer at the top can be switched on to avoid spurious reflections of the gravity wave packet.

In (Rieper et al. 2012) the extended, weakly nonlinear WKB theory by Achatz et al. (2010) is verified, i. e. a WKB model and a full model[5] are compared with respect to the predictions of the WKB theory. Here we recall the major results in short: there is very good agreement for the propagation of wave 1 (initial wave number $\mathbf{k}_0$). The full model shows a wave 2 (wave number $2\mathbf{k}_0$) oscillating about a smoothly increasing amplitude predicted by the WKB theory. For smaller λ, i. e. for smaller ε in the multi-scale asymptotic ansatz, these oscillations vanish. Higher harmonics should not be induced within the orders of magnitude considered in the WKB theory (Achatz et al. 2010) and the full model only produces higher harmonics of a distinctly smaller order of magnitude.

In this text we analyse the behaviour of full and WKB model with respect to numerical

[5]Since the flow remains laminar in the analysed test case in that paper no turbulence model was needed and – without loss of generality – a MUSCL scheme was used.

issues: influence of resolution, flux function, Poisson solver tolerance and the divergence error correction introduced in Sec. 3. Throughout these calculations we used a fixed (small) time step $\Delta t = 1.0$ s in order to fully resolve the buoyancy oscillations. The corresponding CFL numbers depend on the chosen resolution and are stated at due place.

In Fig. 17 it is shown how the various harmonics evolve in time in the full model and according to the WKB theory depending on the *spatial resolution*. Shown are the amplitude maxima of buoyancy for the wave numbers $\alpha \mathbf{k}_0$ with $\alpha = 2, 3, 4$ and 5. The resolution n_λ is given with respect to the number of points per wave length of the initial wave with $\mathbf{k}_0$. The time step of one second leads to a CFL number of 1/60 for the high resolution case and 1/120 for the low resolution case. For the coarse resolution with $n_\lambda = 16$ – corresponding to a domain resolution of $n_x \times n_z = 16 \times 960$ – the wave 2 amplitude falls behind the WKB predicted value. On the other hand the higher harmonics ($\alpha > 2$), which should be absent according to WKB, are of comparable magnitude as wave 2. Obviously, a poor resolution leads to a feed-in of energy from wave 2 to the higher harmonics. If the resolution is doubled (right of Fig. 17) the higher harmonics are clearly of a smaller order of magnitude. If the resolution is doubled again (not shown here) the higher harmonics practically vanish and the WKB predictions are well met. Note that the wave 1 amplitude of the full model (also not shown) always agrees very well with the WKB prediction.

At the resolution $n_\lambda = 32$ the *influence of the flux function* (not shown here) is only marginal. We compare three different flux functions: central difference scheme (CDS), MUSCL and ALDM produce a second harmonic of comparable magnitude. This amplitude is smoothly varying for MUSCL and ALDM but shows a rough evolution for CDS. The differences appear in the higher harmonics. CDS practically does not produce any higher harmonics. MUSCL has very small oscillations in the odd harmonics of $O(1\%)$ of the second harmonic, while ALDM has $O(10\%)$-oscillations in the third harmonic and $O(1\%)$-oscillations in the harmonics higher than 3 for a Poisson-solver tolerance of $\varepsilon = 10^{-9}$.

The *tolerance of the Poisson solver* also influences the spectrum of the solution as can

be seen in Fig. 18. At a tolerance of $\varepsilon = 10^{-5}$ the full model produces spurious amplitudes in the higher harmonics, $\alpha > 1$. Only for small tolerances $\varepsilon < 10^{-6}$ do these harmonics disappear. Note that wave 1 (not shown here) is in good agreement to the WKB predictions for tolerances as large as $\varepsilon = 10^{-5}$. These calculations were done at a high resolution of $n_\lambda = 64$ with a fixed time step of one second and a corresponding CFL number of 1/30.

The tolerance of the Poisson solver can be relaxed if the *divergence-error correction* as described in Sec. 3 is applied. If it is switched off we obtain the result shown in Fig. 19. The higher harmonics do not agree with WKB predictions in contrast to the results shown on the right side of Fig. 18 with the divergence-error correction switched on. Obviously, even wave 1 (left) is completely wrong, see Fig. 19 left. These calculations were also done with $n_\lambda = 64$, a fixed time step of one second and a corresponding CFL number of 1/30.

d. Breaking of a 2D gravity wave packet

With this test we evaluate how the implicit turbulence model handles the breaking of a gravity-wave packet and how the induced turbulence is modelled qualitatively. Since this text focuses on numerical aspects we do not analyse the turbulence characteristics, which is part of future work. The wave packet is initialised as described in Sec. 4 albeit with an amplitude having a Gaussian profile in *two spatial directions* with the initial buoyancy amplitude given by

$$\hat{b}(x,z) = a\frac{N^2}{m}\exp\left[\frac{(z-z_{Center})^2 + (x-x_{Center})^2}{2\sigma^2}\right] \tag{77}$$

with the wave lengths $\lambda_x = \lambda_z = 4$ km and a normalised amplitude factor of $a = 0.9$. The domain is 80 km $\times$ 80 km and resolved with $n_x \times n_z = 640 \times 640$. The time step was fixed to one second leading to a CFL number of 1/6. The background is isothermal with $T_{00} = 300$ K. In Fig. 20 the isolines of the total potential temperature $\theta = \bar{\theta} + \theta'$ are shown at the initial state (top left), after 10 minutes (top right) and in according order after 20, 30, 40 and 50 minutes. Already after 10 minutes the steepening of the gradients becomes visible. The first

overturning of the gravity waves occurs after about 40 minutes. In this text we do not give an analysis of the turbulence modelling but we can see - at least - that the solution remains smooth and physical, grid scale oscillations are avoided by the scheme.

5. Summary and conlusions

We have presented a conservative way of discretising Durran's pseudo-incompressible equations, which was – to the best of our knowledge – until now only done by Smolarkiewicz and Dörnbrack (2008) and by Smolarkiewicz and Szmelter (2011) on unstructured meshes. New is the implementation of a turbulence model right into the numerical flux function. The adaptive local deconvolution method (ALDM) by Hickel (2011); Hickel et al. (2006, 2007) and Hickel and Larsson (2008) is for the first time used in the context of non-Boussinesq flows with a stratified background.

We analyse numerical difficulties and propose ways around them.

- To avoid spurious oscillations and to avoid the activation of the turbulence model on an unperturbed atmosphere, ALDM must only be applied to the deviation $\rho' = \rho - \bar{\rho}$ from the background.

- The physically motivated abort criterion proposed by Smolarkiewicz et al. (1997) for solving the elliptic Helmholtz equation in the context of the Euler equation is adapted to the pseudo-incompressible system.

- To avoid oscillations in a uniform atmosphere at high altitude the Poisson equation has to be scaled with $\bar{\rho}\bar{\theta}$. This causes a height-independent divergence error in the velocity field allowing to reduce the Poisson solver tolerance to acceptable values with respect to the overall computational effort.

- A correction term in the effective continuity equation allows to reduce the number of iterations of the Poisson solver even more. It reduces the effect of the residual

656 divergence error present in the velocity field after the projection step.

657 Note that these methods are applicable to any kind of finite-volume method and are not
658 restricted to the ALDM discretisation. Also note that the implicit turbulence scheme can be
659 switched off. The resulting high order central difference scheme could then be combined with
660 an explicit turbulence model for testing and comparing purposes. In both cases – implicit
661 and explicit – the modelling introduces unresolved subgrid-scale dissipation. The resolved
662 dissipation on the grid scale is done by the discretisation of the viscous stress tensor. Note
663 that this does not lead to "double counting" since turbulence model and physical viscosity
664 act on different scales.

665 With the hot/cold bubble test case by Robert (1993) we validate the code for convective
666 problems. The similarity between the solutions shows two things:

667 • Euler and Durran's equation produce similar results if applied to convective problems.

668 • Upwind schemes and ALDM produce similar results if applied to well resolved laminar
669 flows and ALDM has less numerical dissipation on coarse grids.

670 • The solution only weakly depends on a uniform mean background wind.

671 With the hot bubble test case by Mendez-Nunez and Carroll (1994) we demonstrate the
672 relevance of applying ALDM only to the density perturbations and the capability of the
673 model to cope with convection in the presence of a stratified background.

674 The 1D gravity wave packet (GWP) test case is used to demonstrate the influence of
675 the numerics on the spectral development of a GWP. We compare the results with those
676 predicted by the extended WKB theory (Achatz et al. 2010).

677 • If the resolution is too low, higher harmonics are excited – which is not of physical but
678 only of numerical origin.

679 • The tolerance of the Poisson solver has a direct impact on the spectrum especially on
680 the higher harmonics.

- The introduction of a divergence error correction improves the quality of the spectrum for lower tolerance of the Poisson solver.

In a 2D GWP breaking test case we visualise how the ALDM turbulence model keeps a smooth solution without creating unphysical oscillations on the grid scale. Since this text focuses on numerical issues we do not go further into analysing the turbulence characteristics which is planned for future work.

As turbulence in real GW breaking events is a three-dimensional phenomenon, it remains open to show how a 3D GWP breaks and how the ALDM scheme behaves in such a more physical 3D context. Since calculations in 3D are time consuming this part of the research has to be postponed until a parallel version of pincFloit is available.

So far the model is restricted to the dry atmosphere. We plan to include moist processes in order to be able to study the interaction between gravity waves and clouds. With the implicit turbulence scheme the moist quantities would be transported as a passive tracer, an application for which ALDM has already been tested (Hickel et al. 2007). The latent heat term appears on the right hand side of the divergence constraint.

Acknowledgments.

We thank the Leibniz-Gemeinschaft (WGL) for support within their PAKT programme. S.H. and U.A. thank Deutsche Forschungsgemeinschaft for partial support through the Met-Ström Priority Research Program (SPP 1276), and through grants HI 1273/1-1 Ac71/4-1.

APPENDIX

Momentum flux functions and corresponding density interpolations

a. Momentum fluxes

The momentum fluxes read

$$f^{\rho u}_{i+1/2,j,k} = \hat{\rho}_{i+1,j,k}\left\{\frac{1}{4}(\tilde{u}^{R}_{i,j,k}+\tilde{u}^{L}_{i+1,j,k})^2 - \sigma^{\mathbf{u}}\left|u_{i,j,k}-u_{i+1,j,k}\right|(\tilde{u}^{L}_{i+1,j,k}-\tilde{u}^{R}_{i,j,k})\right\} \tag{A1}$$

$$g^{\rho u}_{i,j+1/2,k} = \hat{\rho}_{i+1/2,j+1/2,k}\left\{\frac{1}{4}(\tilde{u}^{F}_{i,j,k}+\tilde{u}^{B}_{i,j+1,k})(\tilde{v}^{R}_{i,j,k}+\tilde{v}^{L}_{i+1,j,k}) - \sigma^{\mathbf{u}}\left|u_{i,j,k}-u_{i,j+1,k}\right|(\tilde{u}^{B}_{i,j+1,k}-\tilde{u}^{F}_{i,j,k})\right\} \tag{A2}$$

$$h^{\rho u}_{i,j,k+1/2} = \hat{\rho}_{i+1/2,j,k+1/2}\left\{\frac{1}{4}(\tilde{u}^{U}_{i,j,k}+\tilde{u}^{D}_{i,j,k+1})(\tilde{w}^{R}_{i,j,k}+\tilde{w}^{L}_{i+1,j,k}) - \sigma^{\mathbf{u}}\left|u_{i,j,k}-u_{i,j,k+1}\right|(\tilde{u}^{D}_{i,j,k+1}-\tilde{u}^{U}_{i,j,k})\right\} \tag{A3}$$

$$f^{\rho v}_{i+1/2,j,k} = \hat{\rho}_{i+1/2,j+1/2,k}\left\{\frac{1}{4}(\tilde{v}^{R}_{i,j,k}+\tilde{v}^{L}_{i+1,j,k})(\tilde{u}^{F}_{i,j,k}+\tilde{u}^{B}_{i,j+1,k}) - \sigma^{\mathbf{u}}\left|v_{i,j,k}-v_{i+1,j,k}\right|(\tilde{v}^{L}_{i+1,j,k}-\tilde{v}^{R}_{i,j,k})\right\} \tag{A4}$$

$$g^{\rho v}_{i,j+1/2,k} = \hat{\rho}_{i,j+1,k}\left\{\frac{1}{4}(\tilde{v}^{F}_{i,j,k}+\tilde{v}^{B}_{i,j+1,k})^2 - \sigma^{\mathbf{u}}\left|v_{i,j,k}-v_{i,j+1,k}\right|(\tilde{v}^{B}_{i,j+1,k}-\tilde{v}^{F}_{i,j,k})\right\} \tag{A5}$$

$$h^{\rho v}_{i,j,k+1/2} = \hat{\rho}_{i,j+1/2,k+1/2}\left\{\frac{1}{4}(\tilde{v}^{U}_{i,j,k}+\tilde{v}^{D}_{i,j,k+1})(\tilde{w}^{F}_{i,j,k}+\tilde{w}^{B}_{i,j+1,k}) - \sigma^{\mathbf{u}}\left|v_{i,j,k}-v_{i,j,k+1}\right|(\tilde{v}^{D}_{i,j,k+1}-\tilde{v}^{U}_{i,j,k})\right\} \tag{A6}$$

$$f^{\rho w}_{i+1/2,j,k} = \hat{\rho}_{i+1/2,j,k+1/2} \left\{ \frac{1}{4}(\tilde{w}^R_{i,j,k} + \tilde{w}^L_{i+1,j,k})(\tilde{u}^U_{i,j,k} + \tilde{u}^D_{i,j,k+1}) - \sigma^{\mathbf{u}} \left| w_{i,j,k} - w_{i+1,j,k} \right| (\tilde{w}^L_{i+1,j,k} - \tilde{w}^R_{i,j,k}) \right\} \tag{A7}$$

$$g^{\rho w}_{i,j+1/2,k} = \hat{\rho}_{i,j+1/2,k+1/2} \left\{ \frac{1}{4}(\tilde{w}^F_{i,j,k} + \tilde{w}^B_{i,j+1,k})(\tilde{v}^U_{i,j,k} + \tilde{v}^D_{i,j,k+1}) - \sigma^{\mathbf{u}} \left| w_{i,j,k} - w_{i,j+1,k} \right| (\tilde{w}^B_{i,j+1,k} - \tilde{w}^F_{i,j,k}) \right\} \tag{A8}$$

$$h^{\rho w}_{i,j,k+1/2} = \hat{\rho}_{i,j,k+1} \left\{ \frac{1}{4}(\tilde{w}^U_{i,j,k} + \tilde{w}^D_{i,j,k+1})^2 - \sigma^{\mathbf{u}} \left| w_{i,j,k} - w_{i,j,k+1} \right| (\tilde{w}^D_{i,j,k+1} - \tilde{w}^U_{i,j,k}) \right\} \tag{A9}$$

b. Density interpolation

For a consistent discretisation of continuity and momentum equation the density for the momentum flux must be interpolated according to the following equations:

$$f^{\rho u}_{i+1/2,j,k}: \quad \hat{\rho}^n_{i+1,j,k} = \frac{1}{4}(\tilde{\rho}^R_{i,j,k} + \tilde{\rho}^L_{i+1,j,k} + \tilde{\rho}^R_{i+1,j,k} + \tilde{\rho}^L_{i+2,j,k}) \tag{A10}$$

$$g^{\rho u}_{i,j+1/2,k}: \quad \hat{\rho}_{i+1/2,j+1/2,k} = \frac{1}{4}(\tilde{\rho}^F_{i+1,j,k} + \tilde{\rho}^B_{i+1,j+1,k} + \tilde{\rho}^F_{i,j,k} + \tilde{\rho}^B_{i,j+1,k}) \tag{A11}$$

$$h^{\rho u}_{i,j,k+1/2}: \quad \hat{\rho}_{i+1/2,j,k+1/2} = \frac{1}{4}(\tilde{\rho}^U_{i,j,k} + \tilde{\rho}^D_{i,j,k+1} + \tilde{\rho}^U_{i+1,j,k} + \tilde{\rho}^D_{i+1,j,k+1}) \tag{A12}$$

$$f^{\rho v}_{i+1/2,j,k}: \quad \hat{\rho}^n_{i+1/2,j+1/2,k} = \frac{1}{4}(\tilde{\rho}^R_{i,j,k} + \tilde{\rho}^L_{i+1,j+1,k} + \tilde{\rho}^R_{i,j+1,k} + \tilde{\rho}^L_{i+1,j+1,k}) \tag{A13}$$

$$g^{\rho v}_{i,j+1/2,k}: \quad \hat{\rho}^n_{i,j+1,k} = \frac{1}{4}(\tilde{\rho}^F_{i,j,k} + \tilde{\rho}^B_{i,j+1,k} + \tilde{\rho}^F_{i,j+1,k} + \tilde{\rho}^B_{i,j+2,k}) \tag{A14}$$

$$h^{\rho v}_{i,j,k+1/2}: \quad \hat{\rho}_{i,j+1/2,k+1/2} = \frac{1}{4}(\tilde{\rho}^U_{i,j,k} + \tilde{\rho}^D_{i,j,k+1} + \tilde{\rho}^U_{i,j+1,k} + \tilde{\rho}^D_{i,j+1,k+1}) \tag{A15}$$

$$f^{\rho w}_{i+1/2,j,k}: \quad \hat{\rho}_{i+1/2,j,k+1/2} = \frac{1}{4}(\tilde{\rho}^R_{i,j,k} + \tilde{\rho}^L_{i+1,j,k} + \tilde{\rho}^R_{i,j,k+1} + \tilde{\rho}^L_{i+1,j,k+1}) \tag{A16}$$

$$g^{\rho w}_{i,j+1/2,k}: \quad \hat{\rho}_{i,j+1/2,k+1/2} = \frac{1}{4}(\tilde{\rho}^F_{i,j,k} + \tilde{\rho}^B_{i,j+1,k} + \tilde{\rho}^F_{i,j,k+1} + \tilde{\rho}^B_{i,j+1,k+1}) \tag{A17}$$

$$h^{\rho w}_{i,j,k+1/2}: \quad \hat{\rho}^n_{i,j,k+1} = \frac{1}{4}(\tilde{\rho}^U_{i,j,k} + \tilde{\rho}^D_{i,j,k+1} + \tilde{\rho}^U_{i,j,k+1} + \tilde{\rho}^D_{i,j,k+2}) \tag{A18}$$

Reconstruction procedure

What follows is a presentation of the reconstruction procedure. More theoretical background can be found in (Hickel 2008) and the references therein. We make use of the following indices:

$k = 1, 2, 3$	degree of polynomial: constant, linear and quadratic reconstruction
$r = 0, \ldots, k-1$	shift of polynomial, 0 = right most stencil
$l = 0, \ldots, k-1$	specifier index for cell centered variable
$\lambda = -\frac{1}{2}, +\frac{1}{2}$	target position of reconstruction: left or right

The value $\tilde{\phi}$ at the cell interface is the weighted sum over a reconstructed variable $\check{\phi}$, which in turn is calculated from the cell-averaged[6] value $\bar{\phi}$:

$$\check{\phi}_{k,r}(x_{i+\lambda}) = \sum_{l=0}^{k-1} \alpha^{\lambda}_{k,r,l} \bar{\phi}_{i-r+l} \tag{A19}$$

To give an example: The value $\check{\phi}_{3,2}(x_{i+1/2})$ is the value reconstructed in cell i at the right cell face ($\lambda = 1/2$), with a quadratic polynomial ($k = 3$) with the left-most stencil ($r = 2$) consisting of $\bar{\phi}_{i-2}$, $\bar{\phi}_{i-1}$ and $\bar{\phi}_i$ and the corresponding weights $\alpha^{\frac{1}{2}}_{3,2,l}$ with $l = 0, 1, 2$. In general the weights of the filtered values are given by (Hickel et al. 2006)

$$\alpha^{\lambda}_{k,r,l}(x_i) = \Delta x \sum_{m=l+1}^{k} \frac{\displaystyle\sum_{\substack{p=0 \\ p\neq m}}^{k} \prod_{\substack{n=0 \\ n\neq p,m}}^{k} x_{i+\lambda} - x_{i-r+n-\frac{1}{2}}}{\displaystyle\prod_{\substack{n=0 \\ n\neq m}}^{k} x_{i-r+m-\frac{1}{2}} - x_{i-r+n-\frac{1}{2}}}$$

[6]Note that the bar symbolises cell-averaged or filtered value in the appendix and not atmospheric background value as in the main text.

c. Constant reconstruction: k=1

With $k = 1$ we have reconstruction with a constant function as depicted in Fig. 21. The indices can assume the following values

$$r = 0, \quad l = 0, \quad \lambda = \pm\frac{1}{2}$$

and the weights for all reconstruction points $x_{i-1/2}, x_{i+0}$ and $x_{i+1/2}$ are given by

$$\alpha^{\lambda}_{1,0,0} = 1 \qquad \text{for} \quad \lambda = \pm\frac{1}{2} \; .$$

The interpolated values at these points are, as expected of course,

$$\check{\phi}_{k=1,r=0}(x_{i-1/2}) = \bar{\phi}_i \; ,$$

$$\check{\phi}_{k=1,r=0}(x_i) = \bar{\phi}_i \; ,$$

$$\check{\phi}_{k=1,r=0}(x_{i+1/2}) = \bar{\phi}_i \; .$$

d. Linear reconstruction: k=2

The linear reconstruction is depicted in Fig. 22. With $k = 2$ the remaining coefficients take the values

$$r = 0, 1 \qquad l = 0, 1 \qquad \lambda = -\frac{1}{2}, +\frac{1}{2} \; .$$

With some algebra we obtain

$$\alpha^{\lambda}_{2,0,1} = \lambda \; ,$$

$$\alpha^{\lambda}_{2,0,0} = \alpha^{\lambda}_{2,1,1} = 1 + \lambda \; ,$$

$$\alpha^{\lambda}_{2,1,0} = -\lambda \; .$$

The interpolated values for the right stencil is given by

$$\check{\phi}_{k=2,r=0}(x_{i+\lambda}) = \sum_{l=0}^{1} \alpha^{\lambda}_{2,0,l}\bar{\phi}_{i+l} = (1-\lambda)\bar{\phi}_i + \lambda\bar{\phi}_{i+1} \; , \qquad \text{for} \quad \lambda = -\frac{1}{2}, +\frac{1}{2}$$

and for the left stencil by

$$\check{\phi}_{k=2,r=1}(x_{i+\lambda}) = \sum_{l=0}^{1} \alpha^{\lambda}_{2,1,l} \bar{\phi}_{i-1+l} = -\lambda \bar{\phi}_{i-1} + (1+\lambda)\bar{\phi}_i \,, \qquad \text{for} \quad \lambda = -\frac{1}{2}, +\frac{1}{2}$$

e. Quadratic reconstruction: k = 3

The quadratic reconstruction is depicted in Fig. 3. Note that the obtained functions do not interpolate the filtered values $\bar{\phi}$ but the reconstructed point values. The reason therefore is that the cell averaged values $\bar{\phi}$ are related to the antiderivative of ϕ and not to the function itself. The weights for the filtered values are given in the following tableau for $\lambda = \pm 1/2$

$$\begin{aligned}
\alpha^{\lambda}_{3,0,0} &= \frac{1}{2}\lambda^2 - \frac{3}{2}\lambda + \frac{23}{24} && \rightarrow \quad \frac{11}{6}, \frac{1}{3} \\
\alpha^{\lambda}_{3,0,1} &= -\lambda^2 + 2\lambda + \frac{1}{12} && \rightarrow \quad -\frac{7}{6}, \frac{5}{6} \\
\alpha^{\lambda}_{3,0,2} &= \frac{1}{2}\lambda^2 - \frac{1}{2}\lambda - \frac{1}{24} && \rightarrow \quad \frac{1}{3}, -\frac{1}{6}
\end{aligned}$$

$$\begin{aligned}
\alpha^{\lambda}_{3,1,0} &= \frac{1}{2}\lambda^2 - \frac{1}{2}\lambda - \frac{1}{24} && \rightarrow \quad \frac{1}{3}, -\frac{1}{6} \\
\alpha^{\lambda}_{3,1,1} &= -\lambda^2 + \frac{13}{12} && \rightarrow \quad \frac{5}{6}, \frac{5}{6} \\
\alpha^{\lambda}_{3,1,2} &= \frac{1}{2}\lambda^2 + \frac{1}{2}\lambda - \frac{1}{24} && \rightarrow \quad -\frac{1}{6}, \frac{1}{3}
\end{aligned}$$

$$\begin{aligned}
\alpha^{\lambda}_{3,2,0} &= \frac{1}{2}\lambda^2 + \frac{1}{2}\lambda - \frac{1}{24} && \rightarrow \quad -\frac{1}{6}, \frac{1}{3} \\
\alpha^{\lambda}_{3,2,1} &= -\lambda^2 - 2\lambda + \frac{1}{12} && \rightarrow \quad \frac{5}{6}, -\frac{7}{6} \\
\alpha^{\lambda}_{3,2,2} &= \frac{1}{2}\lambda^2 + \frac{3}{2}\lambda + \frac{23}{24} && \rightarrow \quad \frac{1}{3}, \frac{11}{6}
\end{aligned}$$

f. Blending of 1st, 2nd and 3rd-order interpolants

In essentially non-oscillatory (ENO) schemes, a definite polynomial degree k for the interpolant functions is chosen, which determines the spatial order of the scheme. A stencil-

selection algorithm then chooses a stencil r in such a way, as to avoid reconstruction across discontinuities. Contrary to this, weighted essentially non-oscillatory (WENO) schemes use all stencils $r = 0, \ldots, k-1$ of degree k, where the interpolants across discontinuities receive smaller weights than smooth regions, thus keeping oscillations low.

The implicit turbulence model developed by Hickel and Adam makes explicit use of the numerical truncation associated with the reconstruction by polynomials of *all degrees*, $k = 1, 2$ to 3. Thus we sum over all stencils $r = 0, \ldots, k-1$ and all polynomial degrees $k = 1, 2, 3$ to obtain the reconstructed variables at cell faces ($\lambda = \pm\frac{1}{2}$):

$$\tilde{\phi}^{\lambda}(x_{i+\lambda}) = \sum_{k=1}^{3} \sum_{r=0}^{k-1} \omega_{k,r}^{\lambda}(\bar{\phi}, x_i)\ \check{\phi}_{k,r}(x_{i+\lambda})\ ,$$

where $\check{\phi}_{k,r}(x_{i+\lambda})$ are the reconstructed values obtained by Equation (A19). The weights $\omega_{k,r}^{\lambda}(\bar{\phi}, x_i)$ can be chosen to obtain a classical WENO scheme of order $2K-1$, where K is the degree of polynomials used. In ALDM the weights are tuned to represent subgrid-scale turbulence via the truncation error of the various orders of reconstruction. They are defined like

$$\omega_{k,r}^{\lambda}(\bar{\phi}, x_i) = \frac{1}{K} \frac{\gamma_{k,r}^{\lambda} \beta_{k,r}(\bar{\phi}, x_i)}{\sum_{s=0}^{k-1} \gamma_{k,s}^{\lambda} \beta_{k,s}(\bar{\phi}, x_i)}\ . \tag{A20}$$

Note that all polynomial degrees enter the equation with the same weight

$$\sum_{r=0}^{k-1} \omega_{k,r}^{\lambda} = \frac{1}{K}\ .$$

The γ's are tuning parameters and the β's are smoothness indicators given by

$$\beta_{k,r}(\bar{\phi}, x_i) = \left(\varepsilon_{\beta} + \sum_{l=-r}^{k-r-2} (\bar{\phi}_{i+l+1} - \bar{\phi}_{i+l})^2 \right)^{-2}\ , \tag{A21}$$

which are different from their WENO counterparts. The parameter $\varepsilon_{\beta} = 10^{-10}$ avoids devision by 0 in smooth or non-varying regions. We calculate the smoothness indicator for the various instances of k and r.

g. Properties of the γ's

The properties of the 18 parameters γ are given in Hickel (2008) leading to a reduction of the numbers of free parameters down to 4, named here c_1 to c_4. We summarize

$$
\begin{array}{lll}
\boxed{k=1} & \gamma_{1,0}^{-1/2} = c_2 & \gamma_{1,0}^{+1/2} = c_2 \\
\boxed{k=2} & \gamma_{2,0}^{-1/2} = 1 - c_2 & \gamma_{2,0}^{+1/2} = c_2 \\
 & \gamma_{2,1}^{-1/2} = c_2 & \gamma_{2,1}^{+1/2} = 1 - c_2 \\
\boxed{k=3} & \gamma_{3,0}^{-1/2} = 1 - c_3 - c_4 & \gamma_{3,0}^{+1/2} = c_3 \\
 & \gamma_{3,1}^{-1/2} = c_4 & \gamma_{3,1}^{+1/2} = c_4 \\
 & \gamma_{3,2}^{-1/2} = c_3 & \gamma_{3,2}^{+1/2} = 1 - c_3 - c_4
\end{array}
$$

with the coefficients given by

$$
\begin{array}{lll}
c_1 = 0.05003 & c_3 = 0.01902 & \sigma = 0.06891 \\
c_2 = 1.0 & c_4 = 0.0855 &
\end{array}
$$

where σ is a parameter appearing in the definition of the numerical flux function as defined in Section 2 c.

h. Reconstruction weights

1) Constant reconstruction: $\omega_{1,0}$

For the only possible setting $k = 1$ and $r = 0$ we only have one admissible stencil, which leads directly to

$$\omega_{1,0}^{\lambda} = \frac{1}{3} \, .$$

2) Linear reconstruction: $\omega_{2,0}$ and $\omega_{2,1}$

The weights are given by

$$\omega^{\lambda}_{2,0} = \frac{1}{3}\frac{\gamma^{\lambda}_{2,0}\beta_{2,0}}{\gamma^{\lambda}_{2,0}\beta_{2,0} + \gamma^{\lambda}_{2,1}\beta_{2,1}} \qquad \text{and} \qquad \omega^{\lambda}_{2,1} = \frac{1}{3}\frac{\gamma^{\lambda}_{2,1}\beta_{2,1}}{\gamma^{\lambda}_{2,0}\beta_{2,0} + \gamma^{\lambda}_{2,1}\beta_{2,1}} \ ,$$

which can be simplified to $\omega^{-1/2}_{2,0} = \omega^{+1/2}_{2,1} = 0$ and $\omega^{+1/2}_{2,0} = \omega^{-1/2}_{2,1} = 1/3$ using the relations for the γ's.

3) Quadratic reconstruction:$\beta_{3,0}, \beta_{3,1}$ and $\beta_{3,2}$

The sums in Equation (A21) for $\beta_{3,r}$ are given by

$$\beta_{3,0}: \qquad \sum \cdots = (\bar{\phi}_{i+1} - \bar{\phi}_i)^2 + (\bar{\phi}_{i+2} - \bar{\phi}_{i+1})^2 = \Delta\phi^2_{i+1/2} + \Delta\phi_{i+3/2} \ ,$$

$$\beta_{3,1}: \qquad \sum \cdots = (\bar{\phi}_{i} - \bar{\phi}_{i-1})^2 + (\bar{\phi}_{i+1} - \bar{\phi}_{i})^2 = \Delta\phi^2_{i-1/2} + \Delta\phi_{i+1/2} \ ,$$

$$\beta_{3,2}: \qquad \sum \cdots = (\bar{\phi}_{i-1} - \bar{\phi}_{i-2})^2 + (\bar{\phi}_{i} - \bar{\phi}_{i-1})^2 = \Delta\phi^2_{i-3/2} + \Delta\phi_{i-1/2} \ ,$$

yielding a factor

$$\beta_{3,0} = \frac{1}{(\varepsilon + \Delta\bar{\phi}^2_{i+1/2} + \Delta\bar{\phi}^2_{i+3/2})^2} \ ,$$

which indicates that the two participating jumps in the parabolic reconstruction are weighted most if their sum is small, i. e. if the region is smooth. For the weights we obtain

$$\omega^{\lambda}_{3,0} = \frac{1}{3}\frac{\gamma^{\lambda}_{3,0}\beta_{3,0}}{\gamma^{\lambda}_{3,0}\beta_{3,0} + \gamma^{\lambda}_{3,1}\beta_{3,1} + \gamma^{\lambda}_{3,2}\beta_{3,2}} \qquad \cdots$$

REFERENCES

Achatz, U., R. Klein, and F. Senf, 2010: Gravity waves, scale asymptotics, and the pseudo-incompressible equations. *J. Fluid Mech.*, **663**, 120–147.

Adams, N., S. Hickel, and S. Franz, 2004: Implicit subgrid-scale modeling by adaptive deconvolution. *J. Comput. Phys.*, **200 (2)**, 412–431, doi:10.1016/j.jcp.2004.04.010.

Batchelor, G. K., 1953: The conditions for dynamical similarity of motions of a frictionless perfect-gas atmosphere. *Q. J. R. Met. Soc.*, **79**, 224–235.

Durran, D. R. and A. Arakawa, 2007: Generalizing the boussinesq approximation to stratified compressible flow. *Comptes Rendus Mecanique*, **355**, 655–664, doi: 10.1016/j.crme.2007.08.010.

Durran, D. R., 1989: Improving the anelastic approximation. *J. Atmos. Sci.*, **46**, 1453–1461.

Durran, D. R., 2008: A physically motivated approach for filtering acoustic waves from the equations governing compressible stratified flow. *J. Fluid Mech.*, **601**, 365–379, doi:10.1017/S0022112008000608.

Fritts, D. C. and M. J. Alexander, 2003: Gravity wave dynamics and effects in the middle atmosphere. *Rev. Geophys.*, **41 (1)**, 1003, doi:10.1029/2001RG000106.

Gottlieb, S. and C.-W. Shu, 1998: Total variation diminishing Runge-Kutta schemes. *Math. Comput.*, **67 (221)**, 73–85, doi:10.1090/S0025-5718-98-00913-2.

Grabowski, W. W. and T. L. Clark, 1991: Cloud-environment interface instability: Rising thermal calculations in two spatial dimensions. *J. Atmos. Sci.*, **48**, 527–546.

876 Hickel, S., N. A. Adams, and J. Domaradzki, 2006: An adaptive local deconvolution method
877 for implicit LES. *J. Comput. Phys.*, **213 (1)**, 413–436, doi:10.1016/j.jcp.2005.08.017.

878 Hickel, S., N. A. Adams, and N. Mansour, 2007: Implicit subgrid-scale modeling for large-
879 eddy simulation of passive-scalar mixing. *Phys. Fluids*, **19**, 095102.

880 Hickel, S. and J. Larsson, 2008: An adaptive local deconvolution model for compressible
881 turbulence. *Proceedings of the 2008 Summer Program*, Center for Turbulence Research,
882 Stanford University.

883 Hickel, S., M. Mihatsch, and S. J. Schmidt, 2011: Implicit large eddy simulation of cavitation
884 in micro channel flows. *Proceedings of the WIMRC 3rd International Cavitation Forum*,
885 Warwick, UK, ISBN 978-0-9570404-1-0.

886 Hickel, S., 2008: Implicit turbulence modeling for large-eddy simulation. Ph.D. thesis, Tech-
887 nische Universität München.

888 Hickel, S., 2011: Implicit subgrid-scale modeling for large eddy simulations of compressible
889 flows and shock tubulence interaction. *(submitted)*.

890 Klar, J.-U., C. Breitsamter, S. Hickel, and N. A. Adams, 2011: Integrated experimental-
891 numerical analysis of high agility aircraft wake vortex evolution. *J. Aircraft*, **48**, 2050–
892 2058.

893 Klein, R., U. Achatz, D. Bresch, O. M. Knio, and P. K. Smolarkiewicz, 2010: Regime
894 of validity of sound-proof atmospheric flow models. *J. Atmos. Sci.*, **67**, 3226–3237, doi:
895 10.1175/2010JAS3490.1.

896 Klein, R., 2009a: Asymptotics, structure, and integration of sound-proof atmospheric flow
897 equations. *Theor. Comput. Fluid Dyn.*, **23**, 161–195.

898 Klein, R., 2009b: Asymptotics, structure, and integration of sound-proof atmospheric flow
899 equations. *Theoretical and Computational Fluid Dynamics*, **23 (3)**, 161–195.

900 Lindzen, R. S., 1981: Turbulence and stress owing to gravity wave and tidal breakdown. *J.*
901 *Geophys. Res.*, **86**, 9707–9714.

902 Lipps, F. and R. Hemler, 1982: A scale analysis of deep moist convection and some related
903 numerical calculations. *J. Atmos. Sci.*, **29**, 2192–2210.

904 Lipps, F., 1990: On the anelastic approximation for deep convection. *J. Atmos. Sci.*, **47**,
905 1794–1798.

906 Meister, A., 1999: *Numerical methods for linear systems of equations. An introduction to*
907 *modern methods. (Numerik linearer Gleichungssysteme. Eine Einführung in moderne Ver-*
908 *fahren.)*. Braunschweig: Vieweg. x, 222 S. .

909 Mendez-Nunez, L. R. and J. J. Carroll, 1994: Application of the MacCormack scheme to
910 atmospheric nonhydrostatic models. *Mon. Wea. Rev.*, **122**, 984–1000.

911 Ogura, Y. and N. A. Phillips, 1962: A scale analysis of deep and shallow convection in the
912 atmosphere. *J. Atmos. Sci.*, **19**, 173–179.

913 Remmler, S. and S. Hickel, 2012a: Direct and large-eddy simulation of stratified turbulence.
914 *Int. J. Heat Fluid Fl.*, (accepted).

915 Remmler, S. and S. Hickel, 2012b: Spectral structure of stratified turbulence: Direct nu-
916 merical simulations and predictions by large eddy simulation. *Theor. Comp. Fluid Dyn.*,
917 doi:10.1007/S00162-012-0259-9.

918 Remmler, S., 2010: private communication, (TU Munich, 2010).

919 Rieper, F., U. Achatz, and R. Klein, 2012: Validation of an extended non-linear WKB
920 theory: 1D and 2D case. *(submitted to Journal of Fluid Mechanics)*.

921 Robert, A., 1993: Bubble convection experiments with a semi-implicit formulation of the
922 Euler equations. *J. Atmos. Sci.*, **50**, 1865–1873.

923 Shu, C.-W., 1997: Essentially non-oscillatory and weighted essentially non-oscillatory
924 schemes for hyperbolic conservation laws. *ICASE report No. 97-65*.

925 Smolarkiewicz, P. K. and A. Dörnbrack, 2008: Conservative integrals of adiabatic durran's
926 equations. *Int. J. Numer. Methods Fluids*, **56 (8)**, 1513–1519.

927 Smolarkiewicz, P. K., V. Grubišić, and L. G. Margolin, 1997: On forward-in-time differencing
928 for fluids: Stopping criteria for iterative solutions on anelastic pressure equations. *Mon.*
929 *Wea. Rev.*, **125 (4)**, 647–654.

930 Smolarkiewicz, P. K. and L. G. Margolin, 1994: Variational solver for elliptic problems in
931 atmospheric flows. *Appl. Math. Comput. Sci.*, **4 (4)**, 527–551.

932 Smolarkiewicz, P. K. and J. Szmelter, 2011: A nonhydrostatic unstructured-mesh soundproof
933 model for simulation of internal gravity waves. *Acta Geophysica*, **59 (6)**, 1109–1134, doi:
934 10.2478/s11600-011-0043-z.

935 Williamson, J., 1980: Low-storage Runge-Kutta schemes. *J. Comput. Phys.*, **35**, 48–56,
936 doi:10.1016/0021-9991(80)90033-9.

List of Tables

TABLE 1. Average number of iterations of the Poisson solver (BICGSTAB) for the 1D GWP test case, ref. Sec. 4

ε	without div correction	with div correction
10^{-5}	4.8	0.1
10^{-6}	14	0.15
10^{-7}	8.4	0.7
10^{-8}	15	15
10^{-9}	4.6	6.4

List of Figures

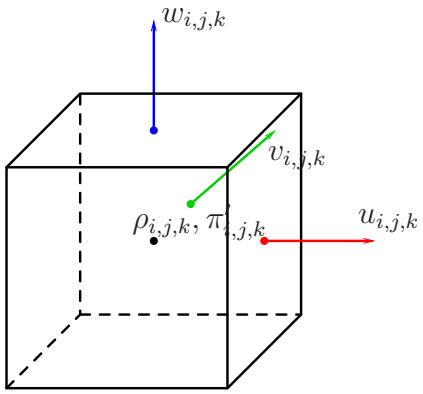

FIG. 1. C-grid variable arrangement in pincFloit.

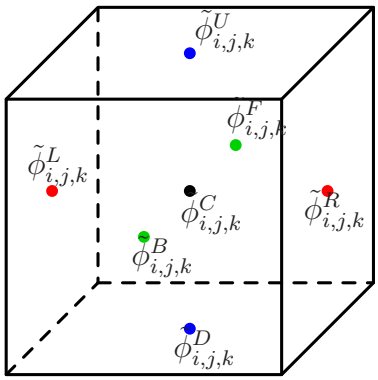

FIG. 2. Position for values from reconstruction in zonal, meridional and vertical direction.

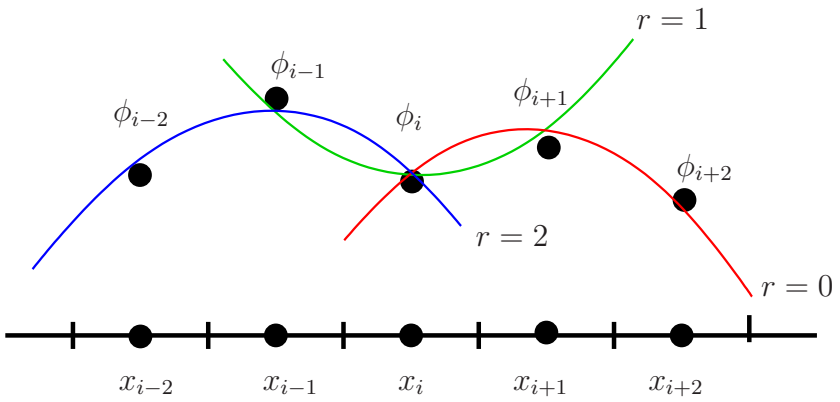

FIG. 3. Three possible reconstructions of ϕ in cell i with quadratic functions from the cell-centred values ϕ.

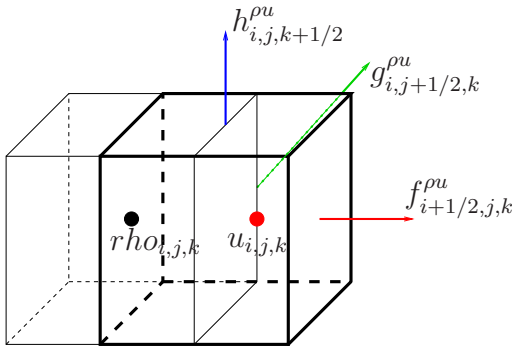

FIG. 4. Location of the ρu-momentum fluxes with respect to the staggered ρu-momentum finite volume grid (grey) and the mass grid (black).

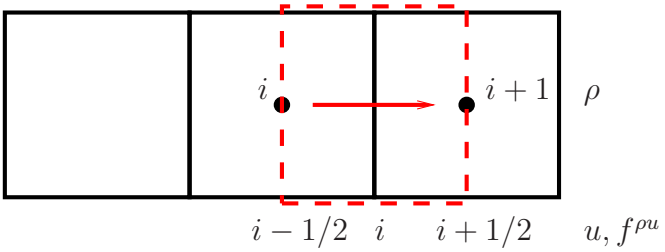

FIG. 5. Position and indices for density, zonal velocity and momentum flux.

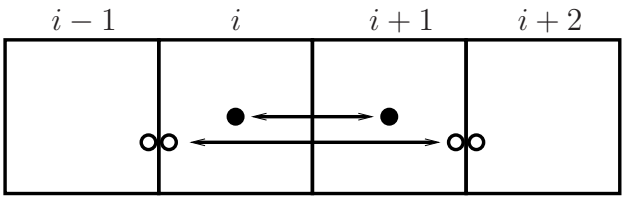

FIG. 6. To achieve consistency between momentum and effective continuity equation the two density differences symbolised with arrows have to be equal. The reconstructed values of the ALDM densities $\tilde{\rho}$ are defined at the position of the hollow circles. The density interpolations $\hat{\rho}$ needed for the momentum flux are situated at the full circles.

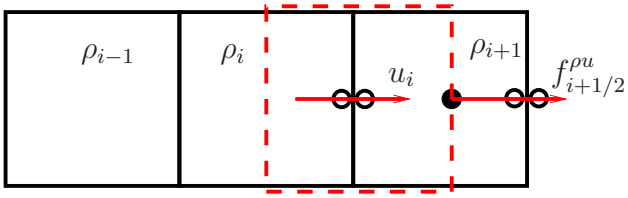

FIG. 7. Illustration of density interpolation rule (21). Position of density $\hat{\rho}$ needed for $f^{\rho u}$ (filled circle) and reconstructed densities for mass flux $\tilde{\rho}$ (empty circle)

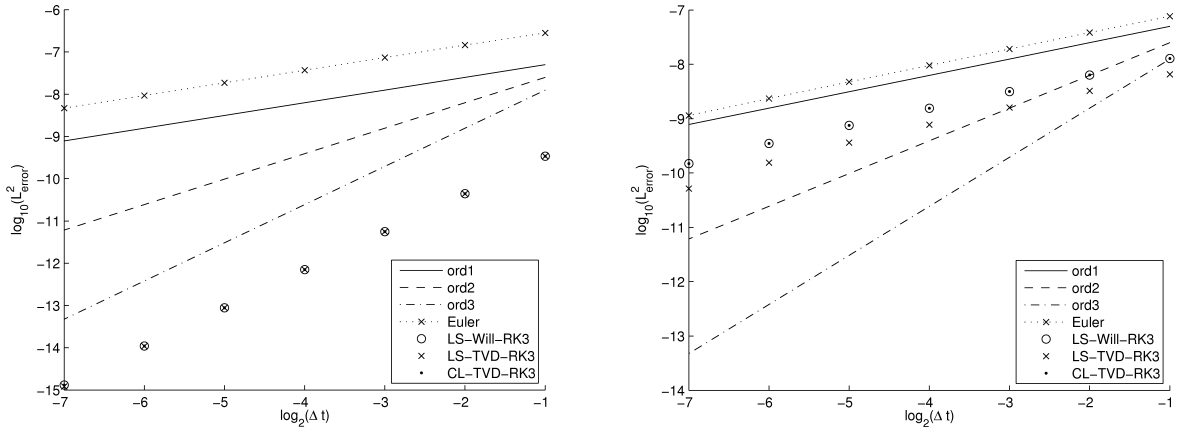

FIG. 8. Convergence study for various time schemes with projection step switched off (left) and with projecting the velocity to satisfy the pseudo-incompressible divergence constraint (right) obtained with the 1D gravity wave packet test case.

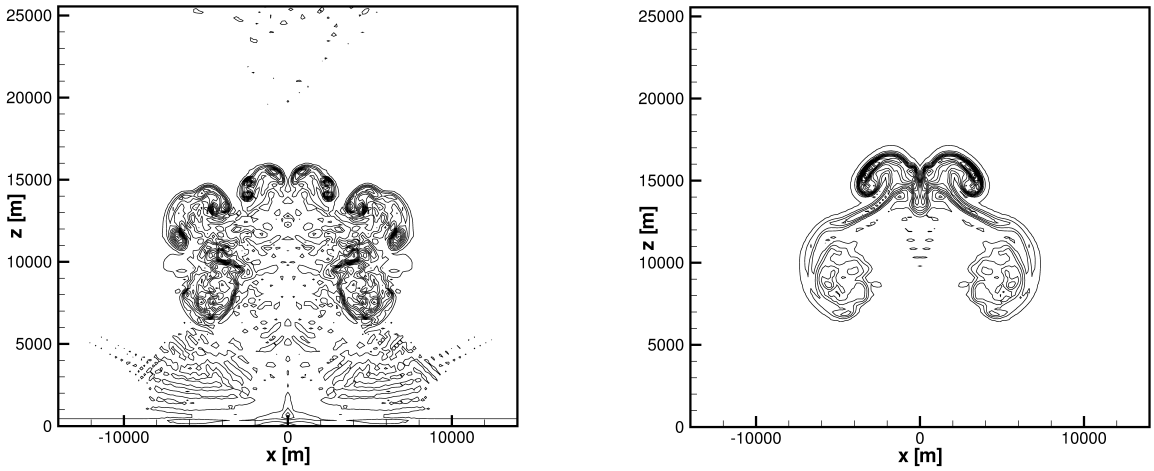

FIG. 9. Isolines of potential temperature for the hot bubble test case at $t = 20$ min. Left: severe oscillations if total density $\rho = \bar{\rho} + \rho'$ is reconstructed width ALDM. Right: ALDM reconstruction only applied to the density fluctuations ρ'.

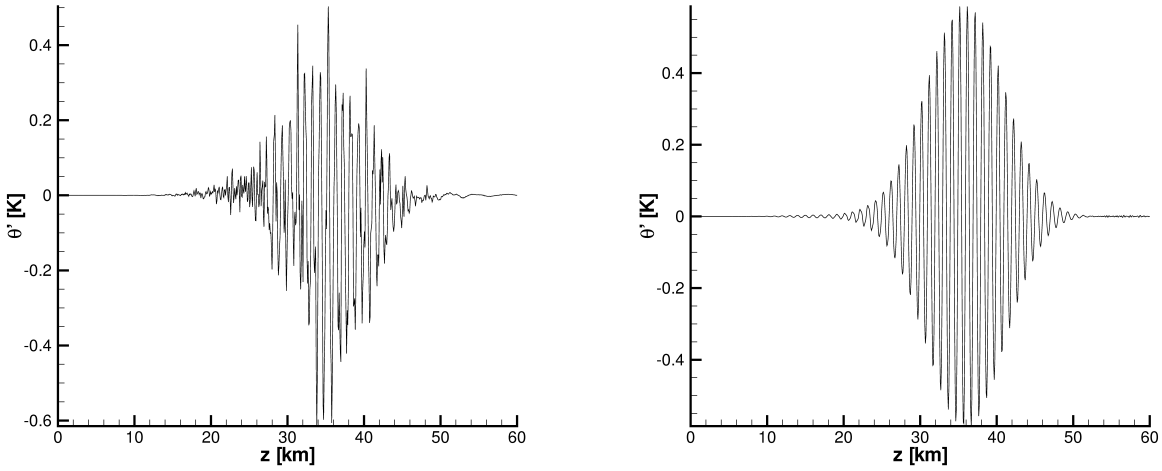

FIG. 10. Potential temperature of 1D gravity wave packet at $t = 150$ min. Left: severe oscillations if total density $\rho = \bar{\rho} + \rho'$ is reconstructed with ALDM. Right: ALDM reconstruction only applied to the density fluctuations ρ'.

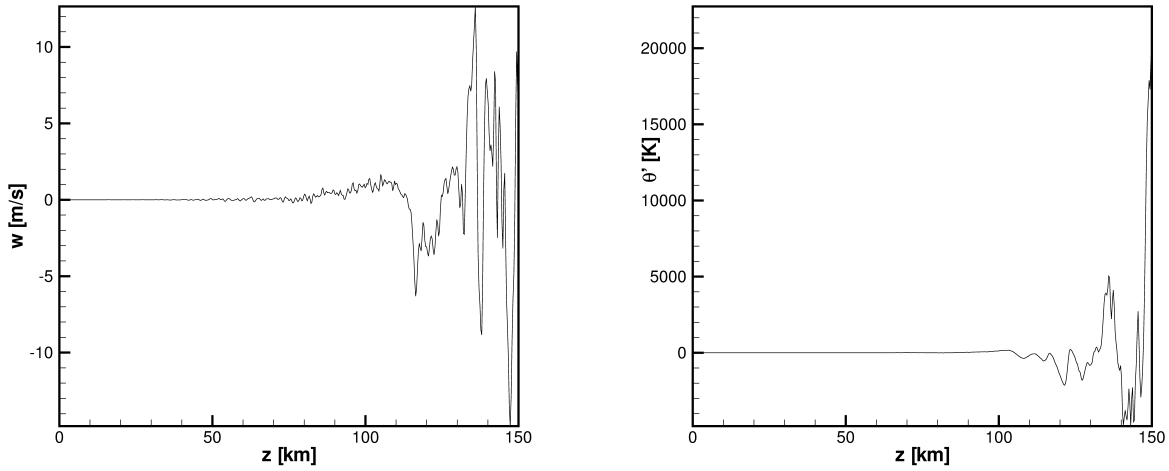

FIG. 11. Fluctuation of vertical velocity (left) and potential temperature (right) in a uniform, isothermal atmosphere at rest due to the divergence error after a few minutes physical time. Poisson equation *without scaling* solved with a tolerance of $\varepsilon = 10^{-7}$.

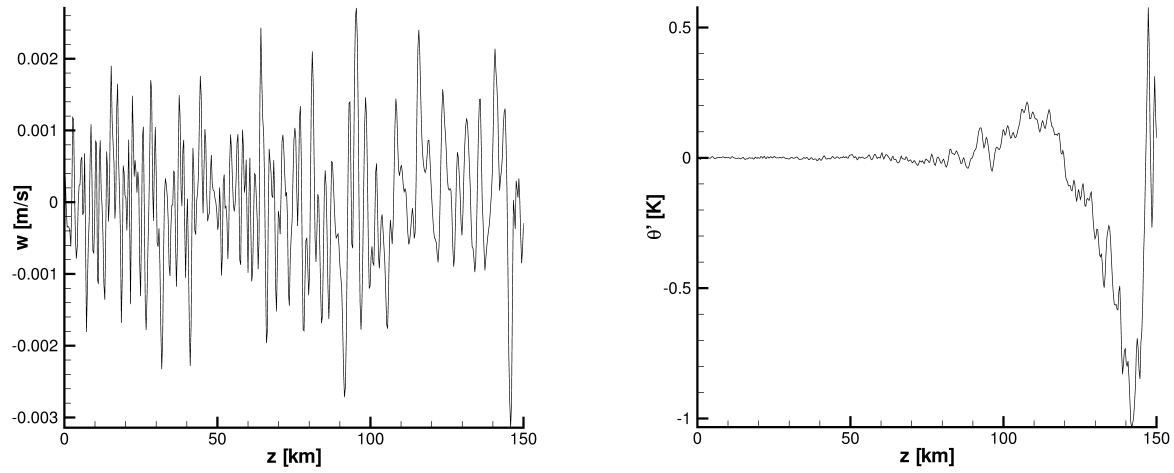

FIG. 12. Fluctuation of vertical velocity (left) and potential temperature (right) in a uniform, isothermal atmosphere at rest due to the divergence error. Poisson equation *with* $\bar{\rho}\bar{\theta}$*-scaling* solved with a tolerance of $\varepsilon = 10^{-7}$.

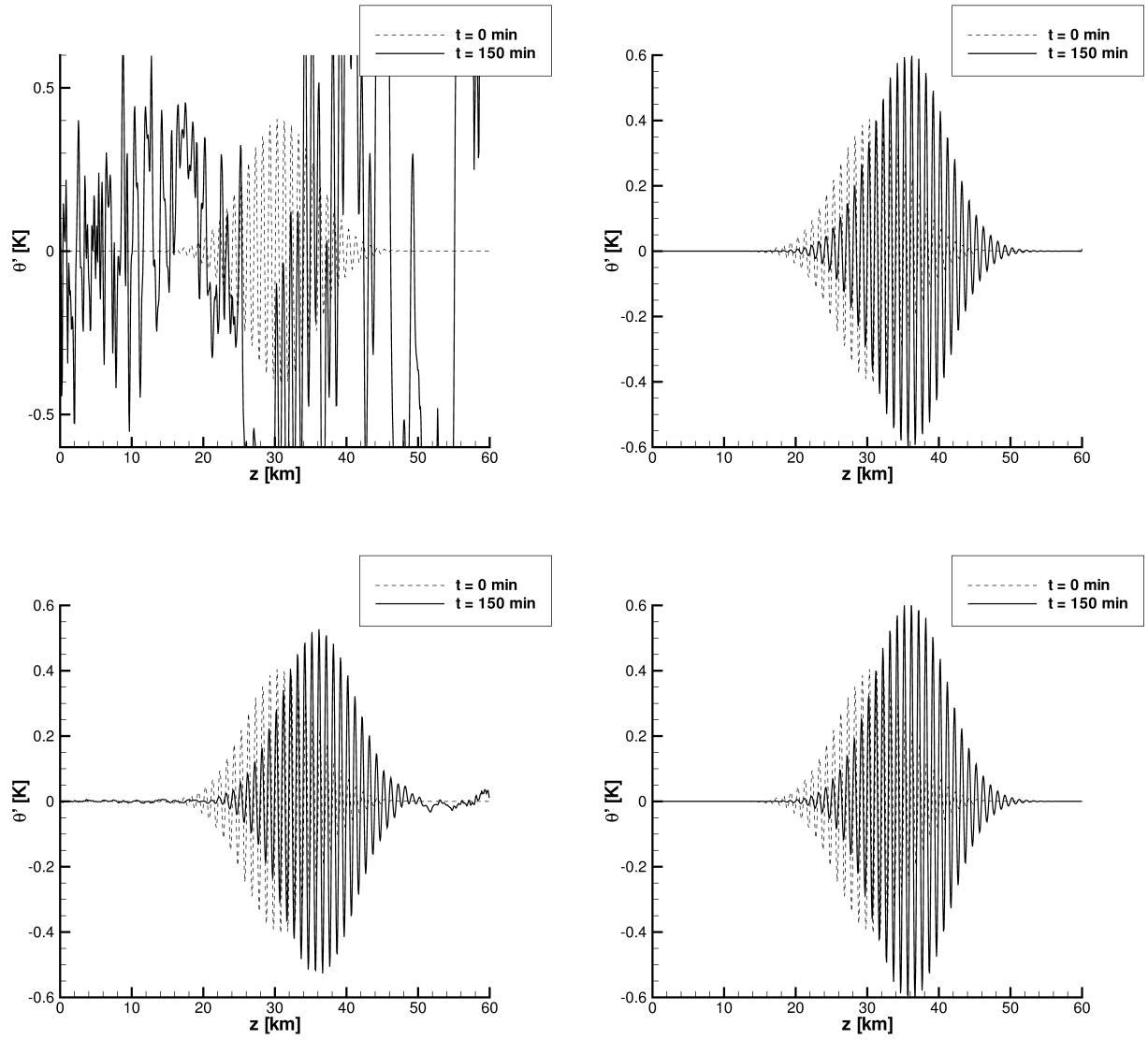

FIG. 13. Potential temperature for the 1D gravity wave packet (see Sec. 4) without divergence error correction (left) and with the divergence error correction as given in Eq. (64) for a Poisson solver tolerance of $\varepsilon = 10^{-5}$ (top) and $\varepsilon = 10^{-7}$ (bottom).

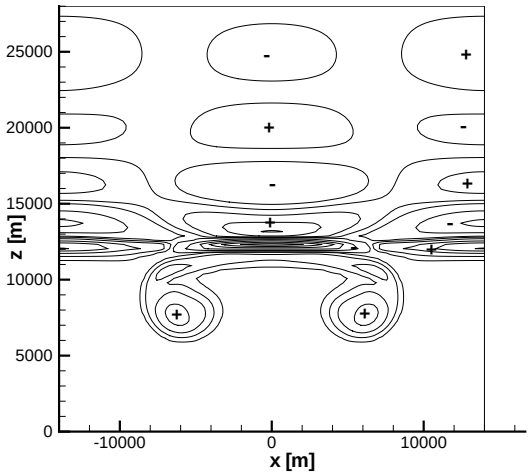

FIG. 14. Isolines of potential temperature perturbation $\theta' = \theta - \bar{\theta}$ for the hot bubble test case with stratification for $z > 12$ km after 20 minutes. The isolines range from -3.2 K to 2.2 K in steps of 0.5 K. Positive perturbations are marked with a "+" and negative perturbations with a "$-$".

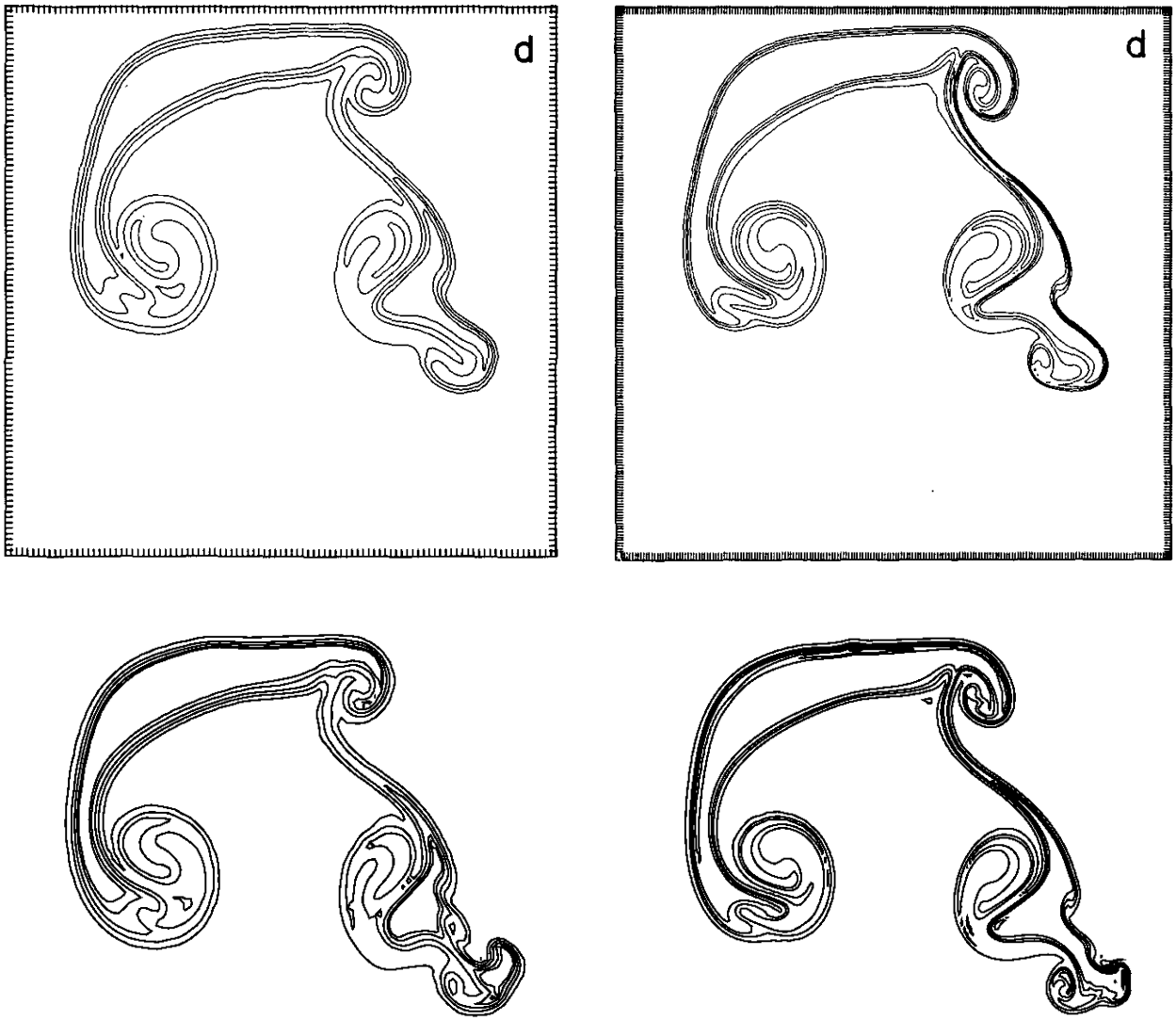

FIG. 15. Isolines of density perturbation $\rho' = \rho - \bar{\rho}$ for Robert's hot/cold bubble test case after 10 min with resolution 100×100 (left) and 200×200 (right) calculated by Robert (1993) with an upwind scheme for the *Euler equations* (top) and calculated with pincFloit, i. e. *pseudo-incompressible equations* with an implicit turbulence model (bottom). The ten isolines are evenly spaced from $\rho' = -2.2$ g m^{-3} to $\rho' = 0.5$ g m^{-3} in steps of $\Delta\rho' = 0.3$ g m^{-3}.

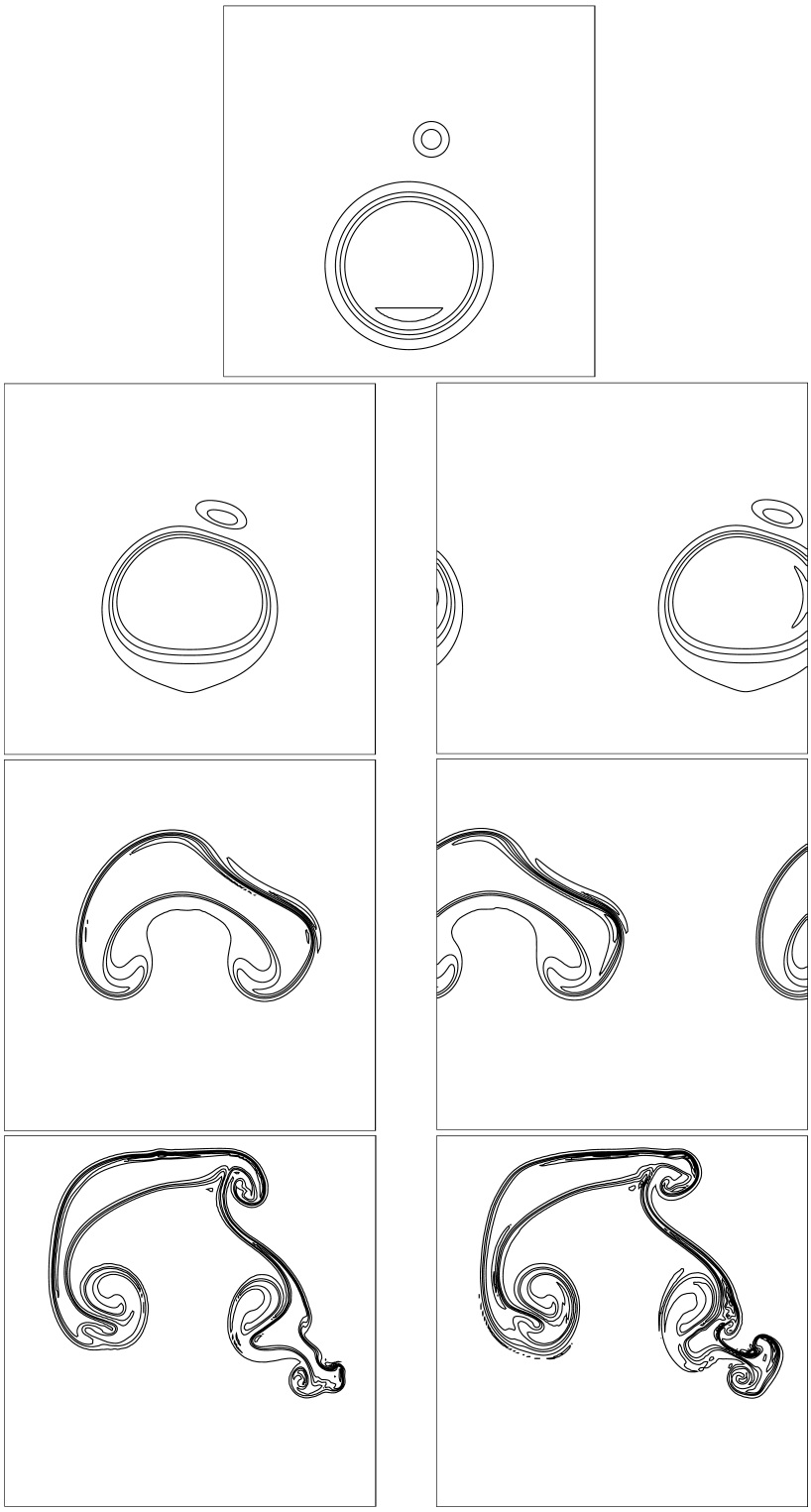

FIG. 16. Isolines of density perturbation for Robert's test case without initial wind (left column) and with a uniform mean wind $u_0 = 1.67$ m s^{-1} (right column). Initial setting (top center), after $\frac{1}{3}10$ minutes (2nd row), after $\frac{2}{3}10$ minutes (3rd row) and after 10 minutes (last row) calculated with ALDM on a 200×200 grid. Spacing of contour lines: from $\rho' = -2.2$ g m^{-3} to $\rho' = 0.5$ g m^{-3} in steps of $\Delta\rho' = 0.3$ g m^{-3}.

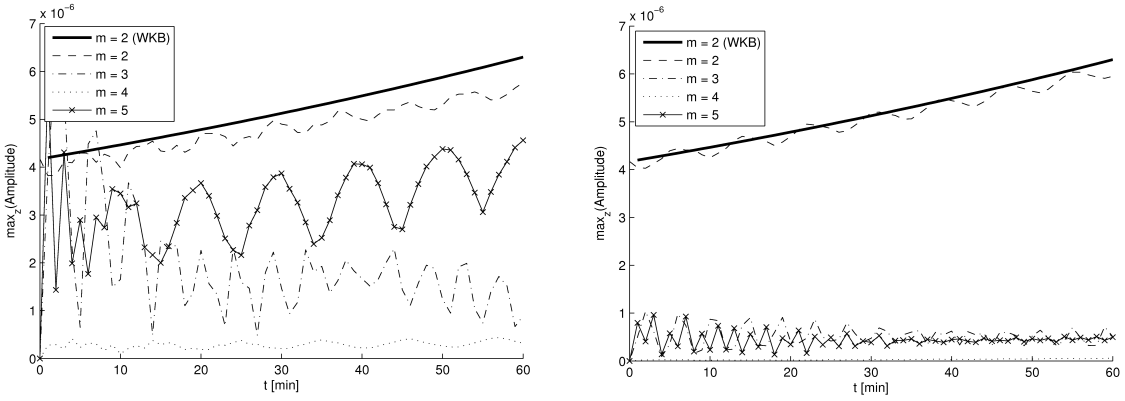

FIG. 17. Amplitude maximum of buoyancy as a function of time for the 1D GWP for wave number 2 to 5 calculated with the full model at a resolution of $n_\lambda = 16$ points per wave length for the initial wave with $\mathbf{k}_0$ (left), $n_\lambda = 32$ (right) and the WKB model (solid line).

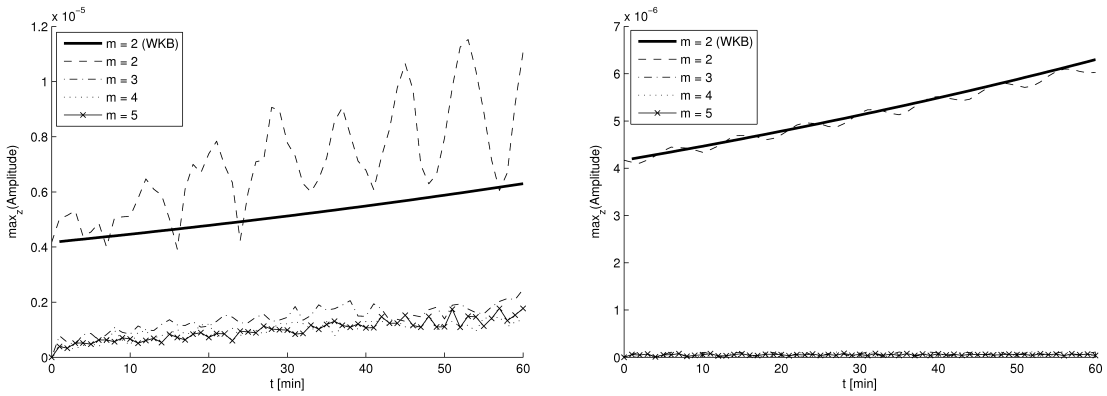

FIG. 18. Amplitude maximum of buoyancy as a function of time for the 1D GWP for wave number 2 to 5 calculated with the full model at a Poisson solver tolerance of $\varepsilon = 10^{-5}$ (left), $\varepsilon = 10^{-7}$ (right) and the WKB model (solid lines).

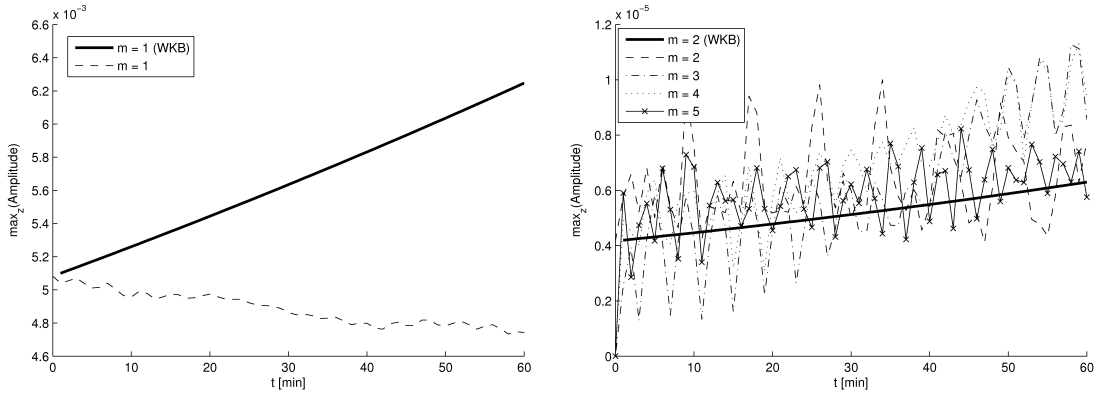

FIG. 19. Amplitude maximum of buoyancy as a function of time for the 1D GWP for wave number 1 (left) and for the higher harmonics 2 to 5 (right) calculated with the full model at a Poisson solver tolerance of $\varepsilon = 10^{-7}$ *without the divergence error correction*. The solid line shows the WKB predicted behaviour.

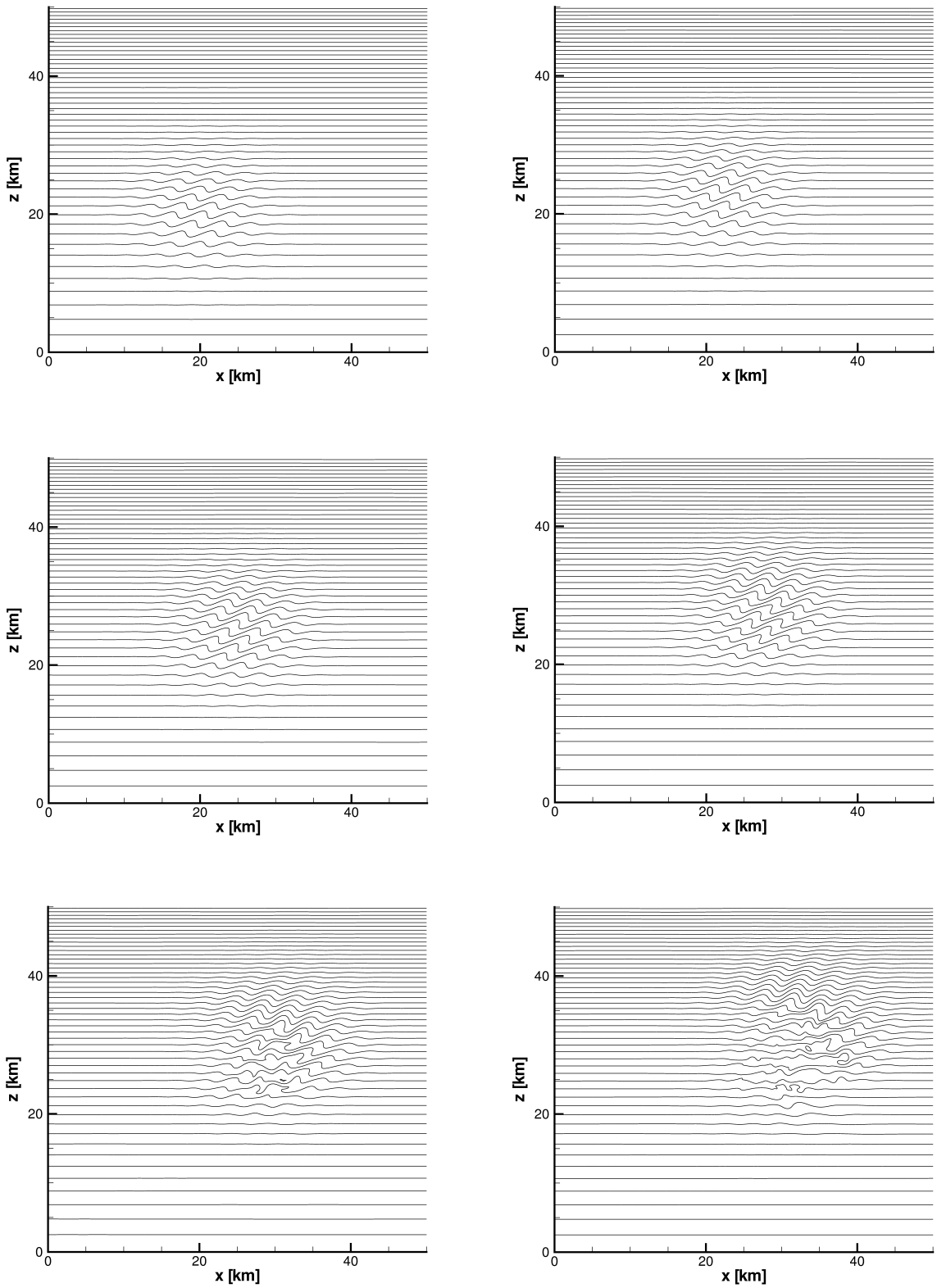

FIG. 20. Isolines of the total potential temperature $\theta = \bar{\theta} + \theta'$ for a breaking 2D gravity wave packet. From left to right and top to bottom after 0, 10, 20, 30, 40 and 50 minutes.

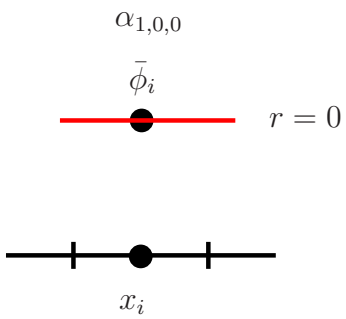

FIG. 21. Reconstruction of ϕ in cell i.

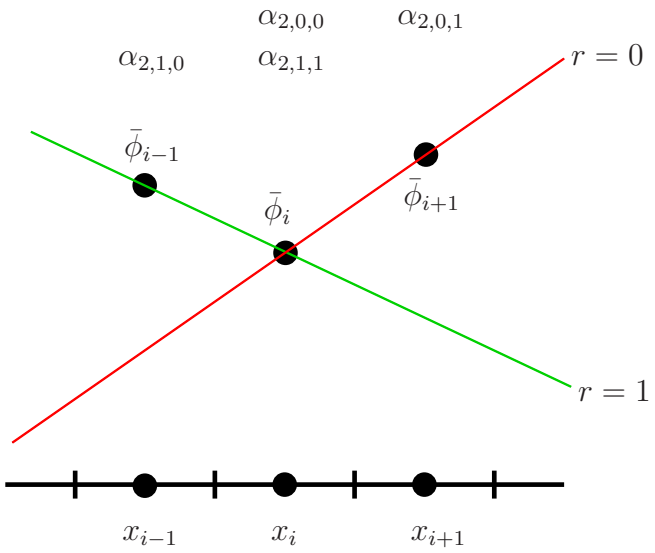

FIG. 22. Two possible reconstructions of ϕ in cell i with linear functions with weights α for corresponding filtered values $\bar{\phi}$.